Progress in $Sp(2N)$ lattice gauge theories

E. Bennett,[a] **J. Holligan,**[b,i,1,*] **D. K. Hong,**[c] **H. Hsiao,**[d,2,*] **J.-W. Lee,**[c,e,3,*]
C.-J. David Lin,[d,f] **B. Lucini,**[g,a,4,*] **M. Mesiti,**[a] **M. Piai**[b] **and D. Vadacchino.**[h,5,*]

[a] *Swansea Academy of Advanced Computing, Swansea University (Bay Campus),*
Fabian Way, SA1 8EN Swansea, Wales, United Kingdom

[b] *Department of Physics, Faculty of Science and Engineering, Swansea University (Park Campus),*
Singleton Park, SA2 8PP Swansea, Wales, United Kingdom

[c] *Department of Physics, Pusan National University, Busan 46241, Korea*

[d] *Institute of Physics, National Yang Ming Chiao Tung University, 1001 Ta-Hsueh Road, Hsinchu 30010,*
Taiwan

[e] *Extreme Physics Institute, Pusan National University, Busan 46241, Korea*

[f] *Center for High Energy Physics, Chung-Yuan Christian University, Chung-Li 32023, Taiwan*

[g] *Department of Mathematics, Faculty of Science and Engineering, Swansea University (Bay Campus),*
Fabian Way, SA1 8EN Swansea, Wales, United Kingdom

[h] *School of Mathematics and Hamilton Mathematics Institute, Trinity College,*
D02 PN40 Dublin 2, Ireland

[i] *Physical Sciences Complex, University of Maryland, College Park, Maryland, USA, 20742*
E-mail: e.j.bennett@swansea.ac.uk, holligan@umd.edu, dkhong@pusan.ac.kr,
thepaulxiao@gmail.com, jwlee823@pusan.ac.kr, dlin@nycu.edu.tw,
b.lucini@swansea.ac.uk, michele.mesiti@swansea.ac.uk,
m.piai@swansea.ac.uk, vadacchd@tcd.ie

Lattice studies of gauge theories with symplectic gauge groups provide valuable information about gauge dynamics, and complement the results of lattice investigations focused on unitary gauge groups. These theories play a central role in phenomenological contexts such as composite Higgs and strongly interacting dark matter models. We report on recent progress of our lattice research programme, starting from the glueball mass spectrum and the topology of the pure gauge theory. We present our results on the mass spectrum of mesons in the quenched approximation, by varying the number of colours in the symplectic group. For the $Sp(4)$ theory, we focus on results obtained with dynamical fermion matter content comprising both fundamental and 2-index antisymmetric representations of the gauge group, as dictated by a well known model of composite Higgs with partial top compositeness.

The 38th International Symposium on Lattice Field Theory, LATTICE2021 26th-30th July, 2021
Zoom/Gather@Massachusetts Institute of Technology

---

[1]Presented *"Sp(4) and Sp(6) quenched meson spectrum,"*combined in this work.

[2]Presented *"Mesonic spectrum of Sp(4) gauge theory with $N_f = 3$ dynamical antisymmetry fermions,"* combined in this work.

[3]Presented *"Sp(4) lattice gauge theory with fermions in multiple representations,"* combined in this work.

[4]Presented *"Sp(2N) gauge theories on the lattice: status and perspectives,"* combined in this work.

[5]Presented *"Topology and scale setting for Sp(2N) pure gauge theories,"* combined in this work.

[*]Speaker

1. Introduction

Our collaboration has been developing an extensive programme of lattice explorations of $Sp(N_c = 2N)$ gauge theories [1–6], reaching far beyond pre-existing explorative and pioneering work on the subject [7]. In the long run, we want to achieve a level of understanding and control over $Sp(2N)$ gauge theories with varying fermionic field content that is comparable to the current state of the art for $SU(N_c)$ theories, and use the results for phenomenological purposes. This contribution reports non-trivial, preliminary results collected over the past year within this research programme, and highlights the next steps of development we envision for the near future.

The main motivation for interest in $Sp(2N)$ gauge theories comes from Composite Higgs Models (CHMs) [8–10]—see the reviews in Refs. [11–13], and the summary tables in Refs. [14–16]. In particular, Ref. [17] highlights how $Sp(2N)$ theories with $N > 1$, and field content consisting of an admixture of Dirac fermions transforming on the fundamental and 2-index antisymmetric representation of the gauge group, provide a compelling origin form CHMs with $SU(4)/Sp(4)$ coset, and naturally incorporate also an enhancement mechanism for the mass of the top through partial compositeness. Importantly, these CHMs can be studied on the lattice with existing technology.

Thanks to the peculiarities of the $Sp(2N)$ groups and their pseudo-real representations, our lattice studies provide an essential contribution to the growing literature on non-perturbative lattice investigations of candidate CHMs. We refer the reader to the literature on lattice theories based on the gauge group $SU(2)$ [18–26] (that yield CHMs with $SU(4)/Sp(4)$ coset, but no top compositeness), and $SU(4)$ [27–32] (which are closely related to CHMs with $SU(5)/SO(5)$ coset), as well as to the recent idea [33] (see also Refs. [34–36]) of using lattice results on the $SU(3)$ theory with $N_f = 8$ fundamental fermions [37–41] to build CHMs with $SU(8) \times SU(8)/SU(8)$ coset.

The beautiful, enhanced symmetry structure of $Sp(2N)$ gauge theories has other applications, prominently in the context of models of dark matter arising from strongly coupled dynamics [42–44]—see for example Refs. [45–50]. More generally, underlying theoretical questions about the nature of gauge dynamics, the mechanism of confinement, the physics of non-trivial bound states such as glueballs, mesons, baryons and more exotic composite objects (such as the chimera baryons described in the body of this paper), and the approach to the large-N_c limit, with its relation to other non-perturbative approaches arising for instance in string theory, are all topics that are amenable to numerical studies within the context of $Sp(2N)$ lattice gauge theories—an incomplete list of relevant references includes Refs. [51–60].

This document is organised as follows. We start with a critical summary of earlier results, which includes new, unpublished material, in Sect. 2. We draw the attention of the reader to the comparison of our results with the most up-to-date literature on $SU(N_c)$ theories. We present a summary plot of the spectrum of the quenched $Sp(4)$ gauge theory, both for glueballs and mesons made of fundamental as well as antisymmetric fermionic matter. After summarising some important technical aspects of our lattice study in Sect. 3.2, we then present our new, preliminary results. In Sect. 3 we discuss the topology of pure Yang-Mills theories with $Sp(2N)$ group for $N = 1, 2, 3, 4$, together with a preliminary extrapolation to the large-N limit, and a comparison with $SU(N_c)$ theories. In Sect. 4 we show the spectra of mesons in the quenched approximations for $Sp(2N)$ theories with $N = 2, 3, 4$, and with fermions in three different representations: the fundamental, the 2-index antisymmetric, and the 2-index symmetric representation.
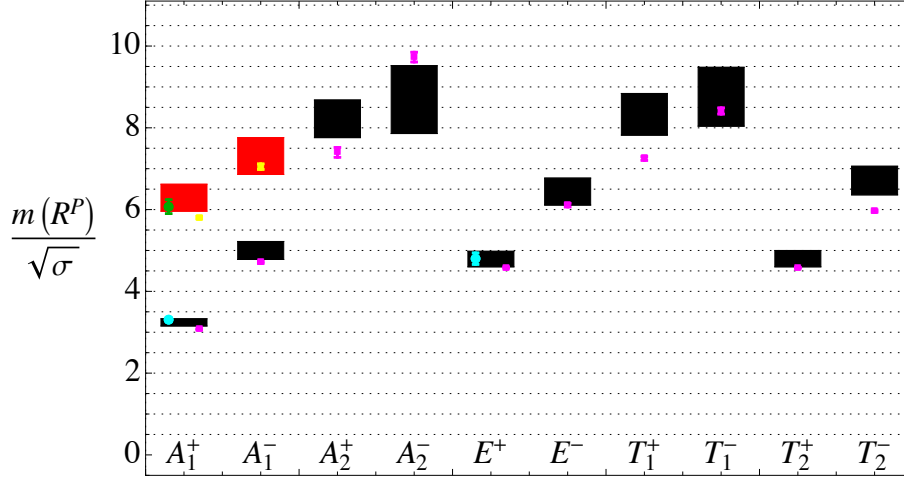
Figure 1: Large-N_c extrapolation of the glueball mass spectrum, in units of the square root of the string tension, for states transforming under irreducible representations of the octahedral group—as indicated along the abscissa. The boxes are our results for $Sp(N_c)$ [6], with the ground states in each channel in black and the measured excitations in red. The points circles are taken from the literature on $SU(N_c)$. In particular, cyan and green points are from Ref. [52], while magenta and yellow points are from Ref. [59].

The theory proposed in Ref. [17] as candidate CHM with top compositeness returns to take central stage in Sect. 5. We focus on the $Sp(4)$ gauge theory with two Dirac fermions in the fundamental representation and three in the antisymmetric representation. We set the stage for the calculation of meson spectra and chimera baryons by first analysing the partially quenched theory (in which fundamental representation fermions are non dynamical), and show our results in Sect. 5.3. Sect. 5.4 contains the first steps of the investigation of the fully dynamical theory, in particular we present a scan of the lattice parameter space relevant for the study of the theory with mixed fermionic content. We conclude with a short outlook in Sect. 6.

2. Critical review of previous work

Prior to the start of our systematic programme of investigation of $Sp(2N)$ lattice theories [1], very little was known numerically about them, available lattice calculations being limited to the Yang-Mills system for $N = 2, 3$ [7].[1] Although motivated by sophisticated CHMs with dynamical matter fields in multiple, distinct representations of the gauge group, we started by first studying simpler theories, that are theoretically better understood and cheaper to simulate, and we gradually built upon these as useful reference points for our subsequent more demanding investigations. In this section, we review the body of work we have produced to date in this programme, highlighting its potential implications, both for phenomenological applications and for theoretical purposes. The order of presentation is chosen to provide a pedagogical way to introduce progressively relevant concepts and observables with increasing level of complexity. Due to space limits, we provide only a discussion of the main results, referring to the original literature for details.

---

[1] The conformal window of $Sp(2N)$ theories had been investigated in Refs. [61, 62]— see also the recent Refs. [63, 64]—and references therein. The EFT description of $Sp(2N)$ gauge theories had been explored for instance in Ref. [65].
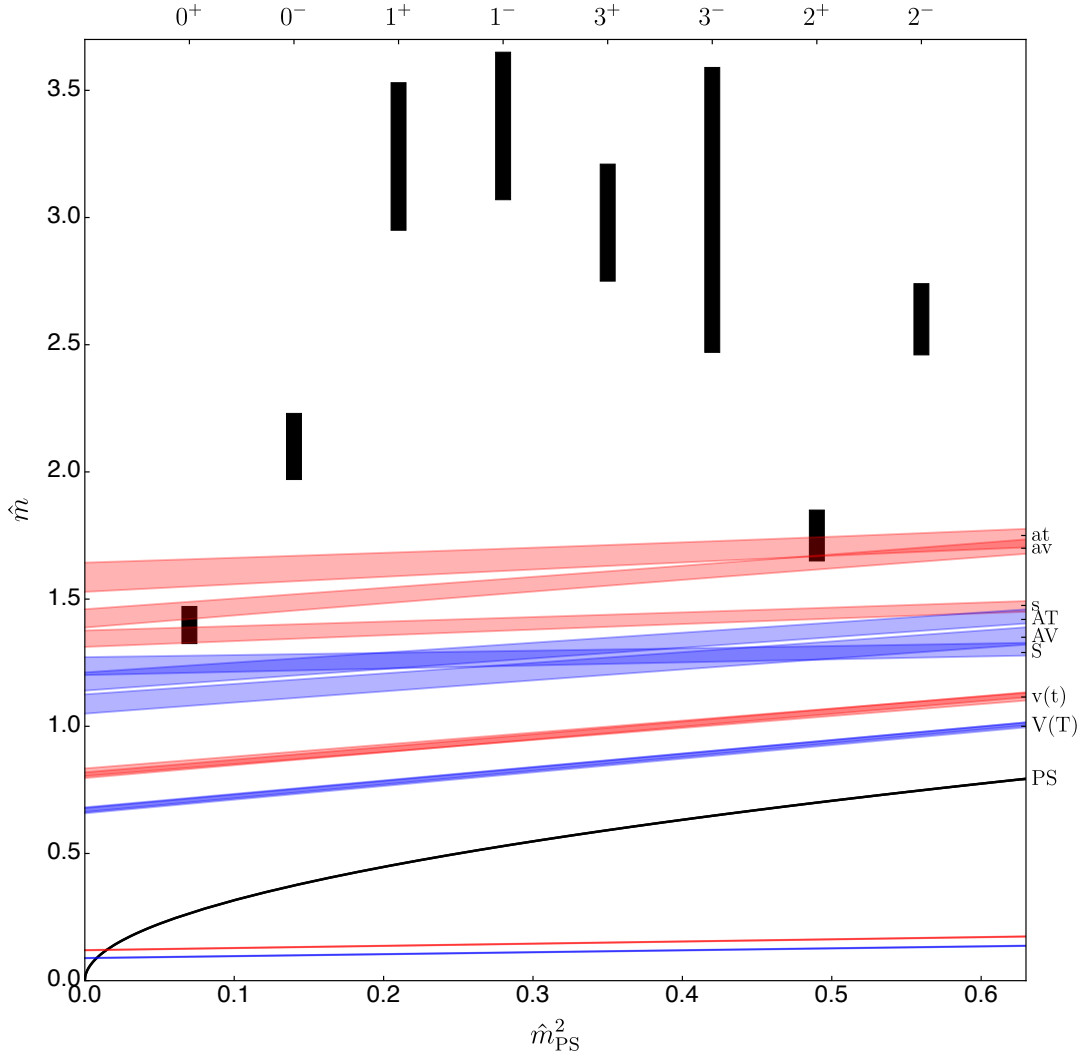
Figure 2: Masses and decay constants of mesons in the quenched approximation for fermions in the fundamental (blue bands) and antisymmetric (red bands) representation of $Sp(4)$, as a function of the pseudoscalar mass squared. Yang-Mills glueball spectra (black boxes) are independent of the pseudoscalar mass, because of the quenched approximation. The pseudoscalar mass is indicated in the plot with a narrow (black) line. Individual mesons are labelled on the right vertical axes. Continuum glueball quantum numbers J^P are indicated on the top horizontal axis.

We start from the Yang-Mills theory. We have determined the continuum limit of the glueball masses in units of the string tension for $N = 2, 3, 4$ and extrapolated those masses to $N \to \infty$. Our results (taken from Ref. [6]) are reported in Fig. 1. We label the states by the irreducible representations of the octahedral group, to which the continuous rotation symmetry reduces on a cubical spatial lattice—see for instance Ref. [53]. Since $Sp(2N)$ groups are pseudoreal, charge conjugation is always positive. The 0^+ glueball is expected to be the lightest state in the A_1^+ irreducible representation, while the 2^+ appears in both the E and the T_2 representations of the octahedral group.

Theories based upon $Sp(N_c)$ and $SU(N_c)$ group sequences are expected to yield observables
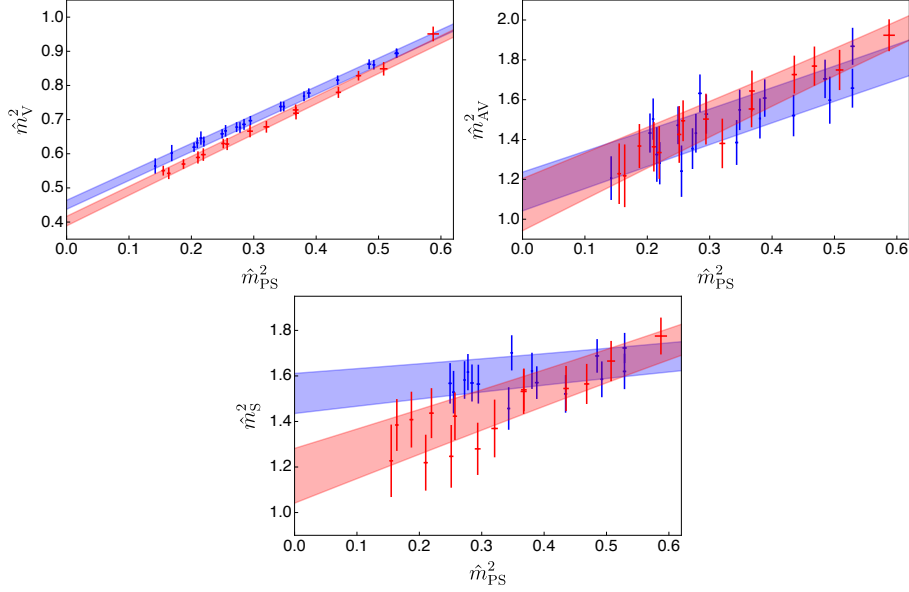
Figure 3: Meson mass squared in the continuum limit as a function of the pseudoscalar mass squared for the vector meson (top left panel), the axial-vector meson (top right) and the flavoured scalar meson (bottom). In blue we represent quenched and in red dynamical data. The bands are extrapolations to the chiral limit.
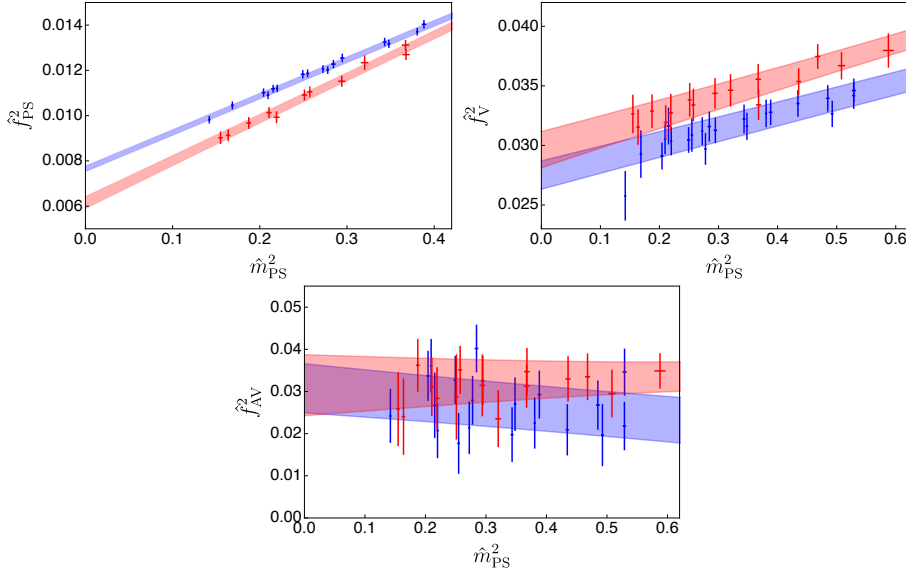

Figure 4: Decay constant squared of the pseudoscalar meson (top left panel), the vector meson (top right) and the axial-vector meson (bottom) in the continuum limit, as a function of the pseudoscalar mass squared. In blue we represent quenched and in red dynamical data. The bands are extrapolations to the chiral limit.

that agree (in the common physical sector) in the large-N_c limit. We can check this explicitly by comparing our calculations to the extrapolations to $SU(\infty)$ done in Refs. [51, 52] (also discussed in [54]). These earlier works report only the lowest-lying states in the spectrum (the ground state 0^{++} and 2^{++}, as well as the excited 0^{++*} state), and Fig. 1 shows good agreement with our results. For the other states in the spectrum, our calculation yield the first determination of the masses in the large-N limit. A large-scale calculation of the $SU(\infty)$ glueball spectrum has appeared recently [59], and we display its results in Fig. 1. While the errors are visibly smaller than ours, the two sets of results are in good agreement, all central values being compatible within two standard deviations.

To get a first sense of the behaviour of the spectrum in the presence of fermions, we have computed masses and decay constants of mesons, in the continuum limit and as a function of the pseudoscalar meson mass, but in the quenched approximation [4]. Fig. 2 displays those quantities together with Yang-Mills glueball masses. We set the scale by the quantity w_0, extracted from the gradient flow as described in Ref. [1]. While the general features of the meson spectrum do not show any striking qualitative representation-dependent features, yet, at fixed pseudoscalar mass, states in the antisymmetric representation are heavier than states in the fundamental representation. Glueballs are generally heavier than mesons in both representations, except that the lightest glueballs have masses comparable to those of the heaviest meson channels we considered.

Dynamical effects due to fundamental representation fermions in masses and decay constants of mesons have been studied in Ref. [3]. We display some representative meson masses in Fig. 3 and decay constants in Fig. 4, again in units of the gradient flow scale w_0. In the range of mass of the pseudoscalar meson currently investigated, unquenching effects are generally small, the only exceptions being the mass of the flavoured scalar and the decay constant of the pseudoscalar meson.

In the rest of this proceedings contribution, we will focus on new, unpublished results, for a large set of observable quantities, and in a broader set of $Sp(2N)$ gauge theories.

3. Topology and Scale setting in $Sp(N_c)$ pure gauge theories

The topological susceptibility of gauge theories is an interesting quantity for several reasons. It enters the Witten-Veneziano formula [66, 67], that explains the large-N_c behavior of the mass of the η' meson. It is the coefficient of the $O(\vartheta^2)$ term in a power expansion of the free energy around $\vartheta = 0$, and as such might have implications for the strong-CP problem. It gives a quantitative account of the importance of instanton configurations in the study of chiral symmetry breaking. As $Sp(N_c)$ gauge groups might be relevant to the UV-completion of composite Higgs and composite dark matter models, the study of their topological susceptibility might find further applications, and furthermore it offers an additional way to compare $SU(N_c)$ and $Sp(N_c)$ theories at large N_c.

The configuration space of gauge fields on a four dimensional torus can be partitioned into topological sectors, each characterized by the value of the topological charge $Q = \int \mathrm{d}^4x q(x)$, where

$$q(x) \equiv \frac{1}{32\pi^2} \epsilon^{\mu\nu\rho\sigma} \mathrm{Tr}\, F_{\mu\nu} F_{\rho\sigma} \;. \tag{1}$$

Q takes values in the third homotopy group of the gauge group, and, since $\pi_3(Sp(2N_c)) = \mathbb{Z}$, we expect Q to be integer valued—as for $SU(N_c)$. The topological susceptibility is defined as

$$\chi = \int \mathrm{d}^4x \langle q(x)q(0) \rangle \;. \tag{2}$$

The evaluation of χ on the lattice is known to be non-trivial for a variety of reasons. First of all, the configuration space of lattice fields is simply connected and its topology is thus trivial; the partitioning of said space in topological sectors arises as a dynamical effect in the vicinity of the continuum limit [68]. Second, as the continuum limit is approached, the lattice topological susceptibility is dominated by quantum UV fluctuations [69]. Lastly, the integrated auto-correlation time of the topological charge is known to diverge as $a \to 0$, and is observed to do so progressively faster as N_c is increased [70].

One way to overcome most of the aforementioned technical difficulties makes use of the gradient flow [71] and its lattice incarnation, the Wilson flow. At finite flow time, the Wilson flow is a smoothened version of the lattice field, which removes UV fluctuations as $a \to 0$, improving the convergence to the continuum limit for the topological susceptibility and other physical quantities. Pure gauge quantities are renormalized at finite flow-time [72]; the value of energy-dependent observables along the flow can also be related to the renormalized coupling calculated in the gradient flow renormalization scheme. The Wilson Flow is thus a natural quantity to use to set the scale of lattice calculations.

The exception is the last of the problems listed above, known as topological freezing, which afflicts the calculations performed near the continuum limit. It is related to the intrinsic difficulty of evolving a global property as the topological charge by a finite sequence of local updates. Dedicated algorithms have been suggested (see, e.g., [73–75]) to address this problem. However, these algorithms are computationally expensive. In our preliminary work, we quantify and monitor the effects of topological freezing through the measurement of the integrated correlation time of the topological charge, which we call τ_Q.

In this section, we report on our preliminary analysis of the properties of the Wilson flow and on the calculation of the topological susceptibility in $Sp(N_c)$ pure gauge theories at finite $N_c = 2N$ and in the $N_c \to \infty$ limit.

3.1 The lattice theory

The $Sp(N_c)$ lattice gauge theory is defined on a four dimensional Euclidean lattice of spacing a by the Wilson action:

$$S_{\mathrm{W}} \equiv \beta \sum_x \sum_{\mu < \nu} \left(1 - \frac{1}{N_c} \operatorname{Re} \operatorname{Tr} \mathcal{P}_{\mu\nu} \right), \tag{3}$$

where x labels the sites, μ and ν the directions on the lattice and $\beta = \frac{2N_c}{g_0^2}$ is the inverse coupling. The quantity $\mathcal{P}_{\mu\nu}(x)$ is called the elementary plaquette:

$$\mathcal{P}_{\mu\nu}(x) \equiv U_\mu(x) U_\nu(x + \hat{\mu}) U_\mu^\dagger(x + \hat{\nu}) U_\nu^\dagger(x), \tag{4}$$

written in term of the link variables $U_\mu(x)$. We consider lattices that have the same linear extent L and periodic boundary conditions in all space-like directions.

3.2 Wilson flow and scale setting for $Sp(N_c)$ gauge theories

The Wilson Flow $V_\mu(t, x)$ is defined as the solution of the equation

$$\frac{\partial V_\mu(t, x)}{\partial t} = -g_0^2 \left\{ \partial_{x, \mu} S_{\mathrm{W}} \left[V_\mu \right] \right\} V_\mu(t, x), \tag{5}$$

with initial condition $V_\mu(0, x) = U_\mu(x)$. It is demonstrated to exist and to be unique on every finite lattice. Since $\partial_t S_W \leq 0$, as the flow-time increases the field tends to configurations that make the action stationary—the classical configurations. Moreover, integrating Eq. (5) is equivalent, at leading order in g_0, to smoothening the field over a sphere of mean-square radius $\sqrt{8t}$. In practice, this can be used to remove short-distance singularities, and the need to introduce counterterms for composite operators. Lastly, it was shown in Ref. [71] that, at leading order in g_0,

$$\alpha(\mu) = k_\alpha t^2 \langle E(t) \rangle = k_\alpha \mathcal{E}(t), \tag{6}$$

where $\alpha(\mu)$ is the renormalized coupling at energy scale $\mu = \frac{1}{\sqrt{8t}}$, k_α is a calculable constant, and $E(t)$ is defined as follows:

$$E(t) = -\frac{1}{2} \operatorname{Tr} \left(G_{\mu\nu} G_{\mu\nu} \right), \tag{7}$$

with $G_{\mu\nu}$ any lattice operator that tends to the field-strength tensor in the continuum limit. Alternative definitions yield differences proportional to powers of the lattice spacing, and are used to estimate the magnitude of discretization errors. In this work, we consider the plaquette operator in Eq. (4) and compare to the four-plaquette clover operator, to this purpose.

The scales t_0 and w_0 are defined by fixing reference values for $\mathcal{E}_0$ and $\mathcal{W}_0$ and solving

$$\mathcal{E}(t_0) = \mathcal{E}_0, \qquad \mathcal{W}(t = w_0^2) = \mathcal{W}_0, \tag{8}$$

where $\mathcal{W}(t) = t \frac{d}{dt} \mathcal{E}(t)$.

But in our study we compute t_0 and w_0 for $Sp(N_c)$ theories with several values of N_c, and we are interested to the ('t Hooft) limit $N_c \to \infty$, reached by holding $\lambda \equiv N_c \alpha$ fixed. Because at leading order in α one expects the perturbative result

$$t^2 \langle E \rangle = \frac{4 C_2(F)}{32\pi^2} \lambda (1 + O(\alpha)) \tag{9}$$

to hold, with $C_2(F) = \frac{N_c+1}{4}$ the quadratic Casimir of the fundamental representation of $Sp(N_c)$, we decided to scale $\mathcal{E}_0$ and $\mathcal{W}_0$ according to the following relations:

$$\mathcal{E}_0 = c_e \frac{N_c + 1}{4}, \qquad \mathcal{W}_0 = c_w \frac{N_c + 1}{4}, \tag{10}$$

where c_e, c_w are constants. Whether this scaling law, suggested by perturbative theory, is reproduced is general is one of the question we start to address in the following.

3.3 Topological charge and susceptibility

The topological charge density at flow-time t is defined as

$$q_L(t, x) \equiv \frac{1}{32\pi^2} \epsilon^{\mu\nu\rho\sigma} \operatorname{Tr} V_{\mu\nu}(t, x) V_{\rho\sigma}(t, x), \tag{11}$$

where $V_{\mu\nu}(t, x)$ is the plaquette operator at flow-time t, built from the solutions of Eq. (5). The topological charge is hence $Q_L(t) = \sum_x q_L(t, x)$. The topological susceptibility is defined as

$$a^4 \chi_L(t) \equiv \left\langle \sum_x q_L(t, x) q_L(t, 0) \right\rangle_\beta = \frac{\langle Q_L(t)^2 \rangle}{L^4}. \tag{12}$$

Table 1: Numerical choices of lattice parameters (N_c, L/a, N_{conf}, β), of the reference values of $\mathcal{E}_0$ and $\mathcal{W}_0$ (rescaled with N_c as explained in the main text) and of our measurements of t_0/a^2, w_0/a, $\chi_L t_0^2$, and $\chi_L w_0^4$.

N_c	L/a	N_{conf}	β	$\mathcal{E}_0$	t_0/a^2	$\chi_L t_0^2$	$\mathcal{W}_0$	w_0/a	$\chi_L w_0^4$
2	12	2000	2.4	0.375	3.455(11)	3.93(12)	0.525	1.9780(47)	3.88(13)
2	16	2000	2.475	0.375	5.609(16)	5.10(17)	0.525	2.4816(50)	5.01(16)
2	20	4000	2.55	0.375	9.095(20)	4.78(11)	0.525	3.1379(47)	4.78(11)
2	24	2000	2.6	0.375	12.490(40)	5.10(19)	0.525	3.6621(77)	5.10(18)
4	20	975	7.7	0.625	4.3620(61)	23.2(1.3)	0.875	2.2645(21)	23.2(1.1)
4	20	2002	7.72	0.625	4.6043(44)	19.63(66)	0.875	2.3281(17)	19.58(63)
4	20	2391	7.76	0.625	5.1101(51)	15.47(44)	0.875	2.4532(17)	15.46(43)
4	20	2002	7.78	0.625	5.3689(63)	14.09(48)	0.875	2.5146(21)	14.04(54)
4	20	2002	7.8	0.625	5.6386(75)	11.79(39)	0.875	2.5766(26)	11.79(40)
4	20	2202	7.85	0.625	6.3559(88)	9.45(39)	0.875	2.7381(27)	9.39(37)
4	24	697	8.2	0.625	13.771(48)	4.56(28)	0.875	4.047(11)	4.59(24)
6	18	952	15.75	0.875	4.1301(47)	15.16(85)	1.225	2.2560(18)	15.39(81)
6	16	499	15.9	0.875	5.014(15)	6.23(43)	1.225	2.4926(54)	6.16(40)
6	16	751	16.1	0.875	6.395(20)	3.70(26)	1.225	2.8235(64)	3.70(25)
6	20	763	16.3	0.875	8.003(18)	4.92(27)	1.225	3.1618(52)	4.90(29)
8	16	1299	26.7	1.125	4.1931(49)	8.71(37)	1.575	2.3129(20)	8.78(36)
8	16	800	27.0	1.125	5.2555(92)	5.60(31)	1.575	2.5949(35)	5.60(29)
8	16	300	27.2	1.125	6.089(22)	3.58(42)	1.575	2.7964(77)	3.54(41)

and is computed from the values of Q_L as measured on the lattice.

General arguments suggest that the sequence of $SU(N_c)$ and $Sp(N_c)$ theories should yield observables (in their common sectors) that agree in the large-N_c limit. One such observable is expected to be the topological susceptibility, and we will next proceed to report our preliminary results for $Sp(2N)$ theories with $N = 1, 2, 3, 4$, and a preliminary extrapolation towards large-N_c.

3.4 Numerical results

Ensembles of thermalized configurations of the lattice $Sp(N_c)$ Yang-Mills theories, at different values of β and L/a for $N_c = 2, 4, 6, 8$, were generated using a heat-bath update algorithm supplemented by over-relaxation, and stored for later analysis. The choices of lattice parameters are reported in the first four columns of Table 1. The value of the number of full lattice sweeps between successive measurements, denoted N_{sw}, was chosen on the basis of preliminary technical runs that were used to determine the auto-correlation time τ_Q; we tuned the choice of N_{sw} in the runs so that $\tau_Q/N_{sw} \lesssim 2$ for every value of β and N_c. These choices ensured that $N_{conf} \sim O(1000)$ topologically uncorrelated configurations be available for each ensemble.

Each configuration is used as the initial condition of the Wilson-flow equation. Numerical integrations are performed with a third-order Runge-Kutta integrator [71]. The range of integration $[0, t_{max}]$ is chosen to avoid finite size effects, with $\sqrt{8t_{max}} < L/(2)$, to obtain the field $V_\mu(t, x)$ for $t < t_{max}$. $\mathcal{E}(t)$ and $\mathcal{W}(t)$ are computed for the plaquette and four-plaquettes clover expressions. The results are displayed in Figure 5—$E(t)$ in the left panel, $W(t)$ in the right one—for three different
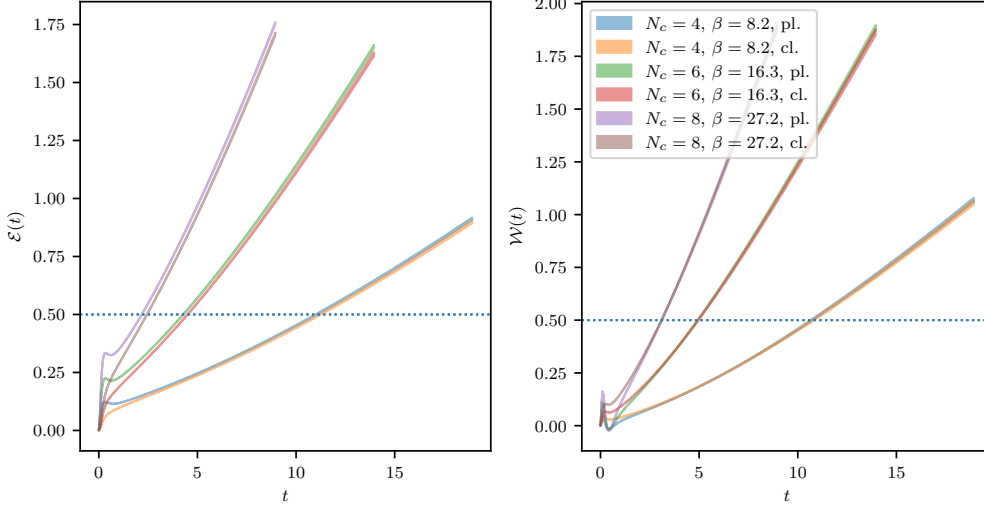
Figure 5: The quantities $\mathcal{E}(t)$—defined in Eq.(6)—and $\mathcal{W}(t) = t\frac{d}{dt}\mathcal{E}(t)$, computed from the plaquette and clover expressions, and obtained from the numerical integration of the Wilson flow equation. Different colours denote different choices of lattice parameters, as in Table 1). The dotted horizontal line denotes an illustrative choice reference value for $\mathcal{E}_0 = \mathcal{W}_0$—not the one used for the measurements.

ensembles, corresponding to the largest available value of β for each of $N_c = 4, 6, 8$. The curves naturally regroup in pairs, corresponds to either the plaquette (pl.) or four-plaquette clover (cl.) choice for $G_{\mu\nu}$. The difference between the two curves in a pair provides an estimate of discretization effects. At sufficiently large value of t, both for $\mathcal{E}(t)$ and $\mathcal{W}(t)$, the difference between the two curves in each pair is roughly a constant. For $\mathcal{W}(t)$, the two curves appear to approach each other, confirming that $\mathcal{W}(t)$ is less affected by discretization effects than $\mathcal{E}(t)$.

To test the validity of the scaling in Eq. (10), we set $c_e = c_w = 0.5$ and compute the corresponding scales t_c and w_c, defined in Eq. (8). We then divide $\mathcal{E}(t)$ and $\mathcal{W}(t)$ by $C_2(F)$, scale the flow time with t_c and w_c^2, and vary N_c. Figure 6, obtained with the largest available values of β, shows that the resulting curves, for $N_c = 4, 6, 8$, agree over a large interval of values of t.

In summary, we have studied the behaviour of the Wilson flow for $Sp(N_c)$ Yang-Mills theories, paying attention both to $\mathcal{E}(t)$ and $\mathcal{W}(t)$. We have identified an interesting, approximate scaling law, suggesting that the values of t_0 and w_0^2 obtained from Eq. (8) only depend on the 't Hooft coupling $\lambda(\mu)$ at scale $\mu = 1/\sqrt{8t}$ and not on N_c. We expect finite-a and large-N_c corrections to alter these (perturbative) scaling properties at smaller β values.

Following Ref. [70], we redefine

$$Q_L(t) \equiv \alpha \sum_x q_L(t, x), \tag{13}$$

where α is determined by numerical minimization of the quantity

$$\Delta(\alpha) = \left\langle \left[\alpha\tilde{Q}_L - \langle \alpha\tilde{Q}_L \rangle \right]^2 \right\rangle. \tag{14}$$

In practice, we find the values of α to be close to unity. The behaviour of $Q_L(t)$ as a function of t for $N_c = 6$ at $\beta = 16.1$ is reported in Figure 7. Other ensembles yield qualitatively similar results:
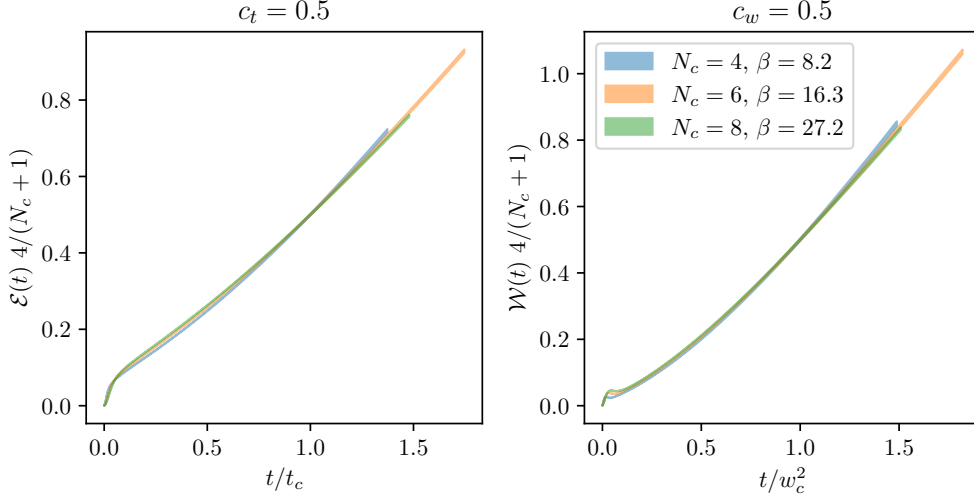
Figure 6: The quantities $\mathcal{E}(t)$—defined in Eq.(6)—and $\mathcal{W}(t) = t\frac{d}{dt}\mathcal{E}(t)$, obtained from numerical integration of the Wilson flow with clover expressions for $E(t)$. Different colours denote different choices of lattice parameters, as in Table 1). With respect to Figure 5, the axes have been rescaled in order to exhibit the scaling of the curves. The vertical axis has been divided by $\frac{N_c+1}{4}$, while the horizontal axis has been rescaled with t_c and w_c^2, measured at the reference values of $\mathcal{E}_0$ and $\mathcal{W}_0$ obtained with Eq. (10), for $c_w = c_e = 0.5$.

after an initial transient, the values of $Q_L(t)$ settle near integer values. This is a residual effect of the fact that we are simulating a discretised system.

In the following, we will use the topological charge obtained from Eq. (11) at fixed flow-time $t = t_0$—defined in Eq. (8)—and corrected according to Eq. (14). For different values of N_c, the reference values $\mathcal{E}_0$ and $\mathcal{W}_0$ were chosen in agreement with Eq. (9), with $c_e = c_w = 0.5$. We will drop the dependence of Q_L on the flow-time from now onwards.

In order to estimate the uncertainty, and monitor the magnitude of topological freezing effects, we compute the integrated auto-correlation time τ_Q of the topological charge. As anticipated, the evaluation of τ_Q allows us to tune N_{sw} so that $\tau_Q/N_{\mathrm{sw}} \lesssim 2$. The calculation can be done in two independent ways: by binning the data and by using Madras-Sokal windowing method [76]. We found agreement in τ_Q obtained with the two different methods, for all the available ensembles. The behaviour of τ_Q in units of the number of full lattice sweeps is represented as a function of $\sqrt{8t_0}/a$ in Figure 8, for different choices of N_c and β. The behaviour of $\ln \tau_Q$ is approximately linear, as in the case of $SU(N_c)$ gauge group [59, 70]. Moreover, the slope in $\ln \tau_Q$ grows as N_c is increased. As N_c is increased, we hence expect topological freezing to set in at smaller values of β, making the continuum extrapolations progressively more computationally expensive, as N_c grows.

Having tuned our choices of N_{sw}, we expect the trajectory of the simulations to sample ergodically the space of configurations, and hence the distribution of Q_L should be symmetric and centered about $Q_L = 0$. This is confirmed but the frequency histogram for Q_L and the simulation history of the topological charge presented in Figure 9, for the ensemble with $N_c = 8$ and $\beta = 27.0$. Other ensembles yield similar behaviors.

The topological susceptibility is computed using Eq. (12) for $t = t_0$. It is represented in units of
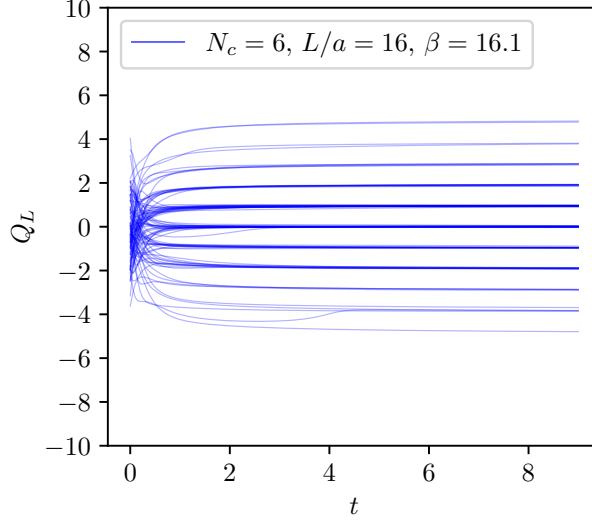
Figure 7: The topological charge defined in Eq. (13) as a function of the flow time t. Each curve corresponds to a different starting configuration in the ensemble with $N_c = 6$, $\beta = 16.1$, and $L/a = 16$. After an initial transient, the values of $Q_L(t)$ approach integer values. Other ensembles yield comparable results.

Table 2: Result of the continuum extrapolation at fixed N_c for $N_c = 2, 4, 6, 8$. The extrapolations are performed according to Eq. (15). The fit results are displayed in Figure 10.

N_c	$\chi_L t_0^2$	$\chi^2/N_{\text{d.o.f.}}$
2	0.002553(81)	0.77
4	0.00227(21)	1.84
6	0.00150(25)	0.72
8	0.00192(59)	1.19

the t_0 scale, as a function of a^2/t_0, in Figure 10. In the same plot we also show the same quantities computed for $SU(N_c)$ gauge theories with open boundary conditions, taken from Ref. [77]. The latter should be less affected by the effects of freezing, and as a result the statistical errors are expected to be much smaller at a similar computational cost [78]. For each value of N_c, we obtain the continuum extrapolation of $\chi_L t_0^2$ by performing a linear fit with

$$\chi_L t_0^2 = t_0 \chi_L(N_c, a = 0) + b_t a^2/t_0, \tag{15}$$

the rests of which are summarised in Table 2, and the large-N_c extrapolation with

$$\chi_L t_0^2 = t_0^2 \chi_L(N_c = \infty, a = 0) + b_N/N_c^2. \tag{16}$$

This simplified, preliminary analysis yields two different values, depending on whether we include or not of the measurements for $N_c = 2$ in the fitting range—see Table 3.

The physics results are somewhat inconclusive, but in the near future we will further refine thee measurements, the extrapolations to continuum and large-N_c limit, and the comparison between $Sp(N_c)$ and $SU(N_c)$ theories, while the results presented in these pages can be considered as a proof
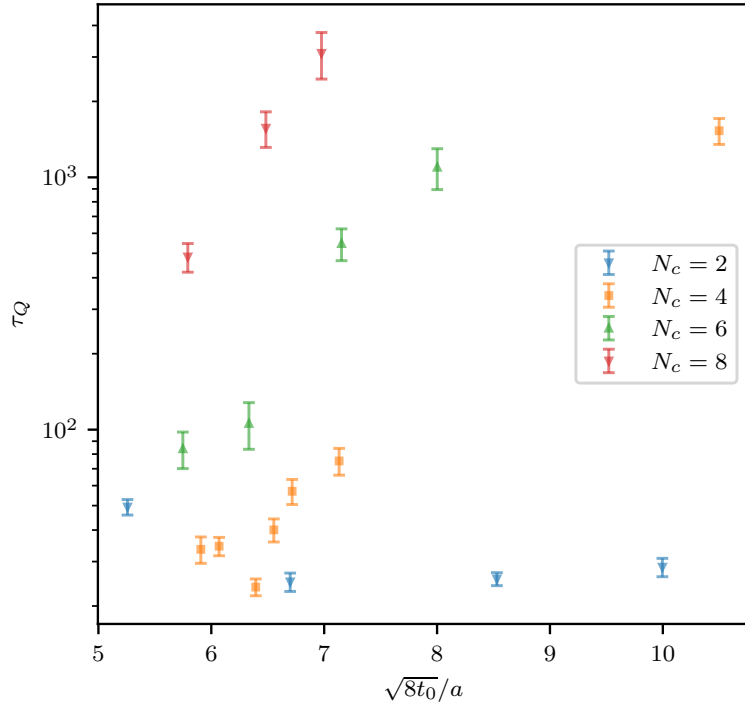
Figure 8: Measurements of τ_Q, obtained with the Sokal-Madras windowing algorithm, as a function of the inverse lattice spacing $\sqrt{8t_0}/a$. Note the log-scale on the vertical axis. As expected from experience with $SU(N)$, τ_Q grows exponentially with $\sqrt{8t_0}/a$.
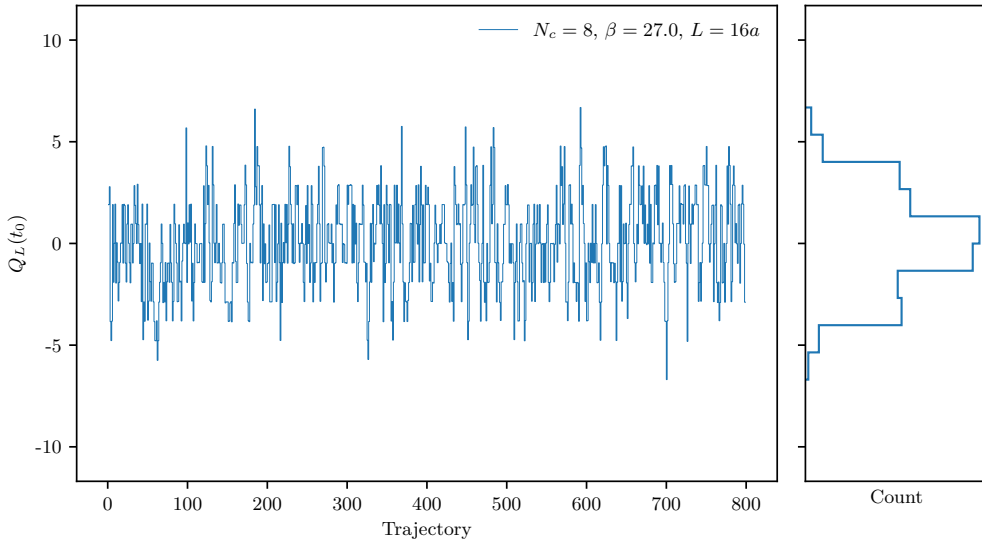
Figure 9: Left panel: the simulation-time history of the topological charge $Q_L(t_0)$ computed from Eq. (13). For these parameters, $\tau_Q = 1.3(2)$. Right panel: the frequency histogram of $Q_L(t0)$. The latter appears to be symmetric and centered around 0, as expected.

13
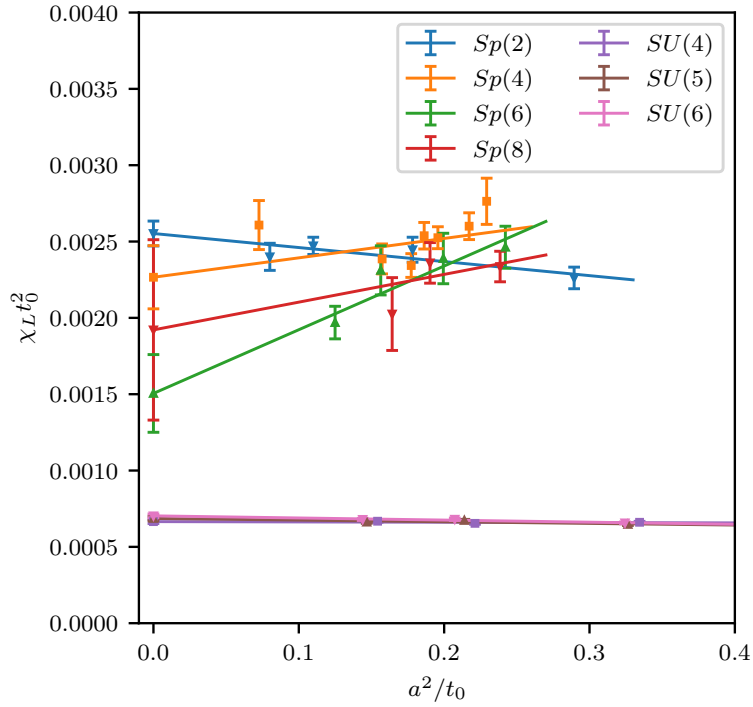
Figure 10: The topological susceptibility $\chi_L t_0^2$, as a function of a^2/t_0, for $Sp(N_c)$ and $SU(N_c)$ gauge theories. The results for $SU(N_c)$ are taken from Ref. [77].

Table 3: Results of the large-N_c extrapolations for $Sp(N_c)$ theories over different fitting ranges, according to Eq. (16). The results of the fits are displayed in Figure 11.

	$\chi_L t_0^2$	$\chi^2/N_{\text{d.o.f.}}$
$N_c > 0$	0.00179(19)	2.01
$N_c > 2$	0.00114(42)	0.99

of principle of our processes. In upcoming publication we will also compare with $SU(N_c)$ results taken from the literature, expressed in units of the square-root of the string tension $\sqrt{\sigma}$, rather than in units of t_0.

4. The quenched meson spectrum

As a first step towards a systematic exploration of phenomenologically interesting models, which may require different choices of $Sp(2N)$ gauge group, we investigate how the mass spectrum of mesons in the quenched approximation changes as we vary N. We adopt the same methodology as in Ref. [4], except that fermions transform in the fundamental (F), or 2-index antisymmetric (AS) or symmetric (S) representations. the dynamics is controlled by the same action in Eq. (3), and we
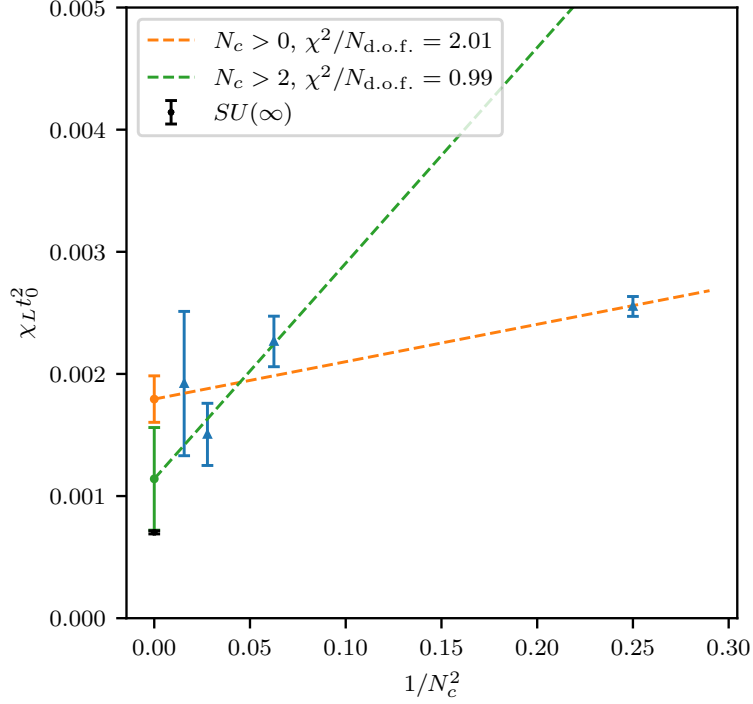
Figure 11: Preliminary results for the continuum extrapolation of the topological susceptibility $\chi_L t_0^2$ for $Sp(N_c)$ gauge theories as a function of $1/N_c^2$. The results are extrapolated to $N_c \rightarrow \infty$ using the ansatz $\chi_L t_0^2 = a + b/N_c^2$ for $N_c > 2$ (green) or $N_c > 0$ (orange). The result of the extrapolation to $N_c = \infty$ for $SU(N_c)$ gauge theories, taken from Ref. [77], is represented as a black bullet.

define the massive Wilson Dirac operators for (quenched) fermions ψ in the representation R to be

$$D^R \psi(x) \equiv \left(\frac{4}{a} + m_0^R \right) \psi(x) - \frac{1}{2a} \sum_\mu \left\{ (1 - \gamma_\mu) U_\mu^R(x) \psi(x + \hat\mu) + \right.$$
$$\left. + (1 + \gamma_\mu) U_\mu^{R\,\dagger}(x - \hat\mu) \psi(x - \hat\mu) \right\}, \tag{17}$$

where m_0^R is the bare fermion mass, a the lattice spacing, and $\hat\mu$ a unit vector in direction μ on the lattice. For the F representation we denote the gauge link as $U_\mu^F = U_\mu \in Sp(2N)$. For the 2-index representations we construct the link variables as follows [79]:

$$\left(U_\mu^R \right)_{(ij),\,(kl)} (x) = \text{Tr} \left[(e_R^{(ij)})^\dagger U_\mu(x) e_R^{(kl)} U_\mu^T(x) \right], \quad \text{with } i < j, \; k < l. \tag{18}$$

For $R = S$ and $R = AS$ the orthonormal basis e_R is given by symmetric and antisymmetric $2N \times 2N$ matrices, respectively. For symplectic groups, e_{AS} further satisfies $\text{Tr}[\Omega e_{AS}] = 0$, with Ω the symplectic matrix.

We list in Table 4 the interpolating operators used to compute the spectrum of mesons with spin J and parity P. They are built by combining spinors ψ and $\overline\psi \equiv \psi^\dagger \gamma^0$ with different Dirac structures. The labels PS, S, V, AV, T, and AT stand for pseudoscalar, scalar, vector, axial-vector, tensor, and axial-tensor, respectively. We display the corresponding QCD mesons to facilitate comparison.

Table 4: Interpolating operators O_S used to construct meson states, with their labels and quantum assignments. The indices $i \neq j$ denote flavours, while colour and spin indexes are implicit. The corresponding mesons in QCD are included for comparison.

Label	O_M	J^P	QCD meson
PS	$\overline{\psi^i}\gamma^5\psi^j$	0^-	π
S	$\overline{\psi^i}\psi^j$	0^+	a_0
V	$\overline{\psi^i}\gamma^\mu\psi^j$	1^-	ρ
AV	$\overline{\psi^i}\gamma^5\gamma^\mu\psi^j$	1^+	a_1
T	$\overline{\psi^i}\gamma^0\gamma^\mu\psi^j$	1^-	ρ
AT	$\overline{\psi^i}\gamma^5\gamma^0\gamma^\mu\psi^j$	1^+	b_1

The physical observables—masses and decay constants—are extracted by examining the appropriate two-point correlation functions between two distinct coordinates on the lattice. Writing the generic operator as $O_M(x) = \overline{\psi^i}(x)\Gamma^M\psi^j(x)$, the correlators are defined as

$$C_{MM'}(x-y) = \langle O_M(x)O_{M'}^\dagger(y)\rangle = -\mathrm{Tr}\left[\Gamma^M D_{R,i}^{-1}(x-y)\Gamma^{M'}D_{R,j}^{-1}(y-x)\right], \qquad (19)$$

where $D_{R,i}^{-1}(x-y)$ is the inverse of the Dirac operator from Eq. (17), for fermion representation R and flavor index i. The fermions transform in the same representation of the gauge group, to form a gauge singlet, but we restrict our attention to flavoured mesons, with $i \neq j$.

We call $C_M(t)$ the spatially-averaged correlator with $M = M'$, at asymptotically large time separation $t \to \infty$, which behaves as

$$C_M(t) \to \frac{|\langle 0|O_M|M\rangle|^2}{2m_M}\left[e^{-m_M t} + e^{-m_M(T-t)}\right], \qquad (20)$$

where m_M is the mass of the meson in the ground state $|M\rangle$ and T is the the temporal extent of the lattice. To extract the decay constants of the PS, V and AV states, we use the following parametrisations of the matrix elements for (partially) conserved currents:

$$\langle 0|\overline{\psi^i}\gamma^5\gamma^\mu\psi^j|PS\rangle \equiv \sqrt{2}f_{PS}p^\mu, \qquad (21)$$
$$\langle 0|\overline{\psi^i}\gamma^\mu\psi^j|V\rangle \equiv \sqrt{2}f_V m_V \epsilon^\mu, \qquad (22)$$
$$\langle 0|\overline{\psi^i}\gamma^5\gamma^\mu\psi^j|AV\rangle \equiv \sqrt{2}f_{AV}m_{AV}\epsilon^\mu, \qquad (23)$$

where the decay constant f_{PS} is normalised so that it would yield $f_\pi \simeq 93\,\mathrm{MeV}$ in QCD. p^μ and ϵ^μ are the momentum and polarisation four-vectors, respectively. They obey $\epsilon^\mu p_\mu = 0$ and $\epsilon^\mu \epsilon_\mu = 1$. These definitions, together with Eq. (20), suffice to extract all measurables from lattice results, except for f_{PS}. We further need one more correlation function:

$$C_{AV,PS}(t) = \sum_{\vec{x}}\langle 0|O_{AV}(\vec{x},t)O_{PS}^\dagger(\vec{0},0)|0\rangle \xrightarrow{t\to\infty} \frac{\sqrt{2}f_{PS}\langle 0|O_{PS}|PS\rangle^*}{2}\left[e^{-m_{PS}t} - e^{-m_{PS}(T-t)}\right].$$
$$(24)$$

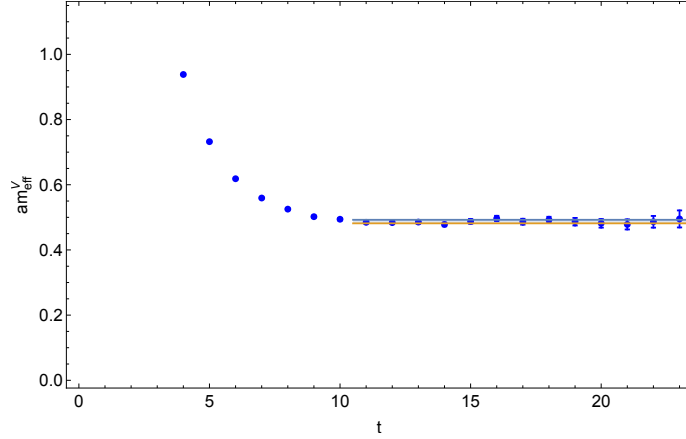We extract f_{PS} from the simultaneous fits to Eqs. (20) and (24).

16

Figure 12: An example of effective mass plotted against Euclidean time for $Sp(4)$. The width of orange and blue lines are the selected time-interval and the vertical distance between them corresponds to the statistical error in the measurement. This measurement uses lattice size 48×24^3, coupling $\beta = 7.62$, and bare Wilson mass $am = -0.78$. the fit that has $\chi^2/N_{d.o.f} = 0.84$.

The effective mass $am_{\text{eff}}(t)$ is a function of Euclidean time t. We seek a late-time plateau in the effective mass and restrict our fits to a region in which $am_{\text{eff}}(t)$ is approximately constant. An example is shown in Fig. 12 for the effective mass of vector meson V in the quenched $Sp(4)$ on a 48×24^3 lattice, where the lattice parameters are $\beta = 7.62$ and $am_0 = -0.78$. The plateau starts at $t = 11$. In the figure we also show the result obtained from curve-fitting, denoted by solid lines.

The decay-constants require renormalisation, even in the quenched approximation in which we neglect fermion loops. The process introduces multiplicative factors in each meson channel:

$$f_{PS}^{\text{ren}} = Z_A f_{PS}^{\text{bare}}, \quad f_V^{\text{ren}} = Z_V f_V^{\text{bare}}, \quad f_{AV}^{\text{ren}} = Z_A f_{AV}^{\text{bare}}. \tag{25}$$

For $Sp(N_c)$, the two Z quantities are calculated in lattice perturbation theory for Wilson fermions at the one-loop level [80], along with tadpole improvement [81], and given by

$$Z_V = 1 + C_2(R)(\Delta_{\Sigma_1} + \Delta_{\gamma_\mu})\frac{N_c}{8\pi^2\beta\langle P\rangle}, \tag{26}$$

$$Z_A = 1 + C_2(R)(\Delta_{\Sigma_1} + \Delta_{\gamma_5\gamma_\mu})\frac{N_c}{8\pi^2\beta\langle P\rangle}. \tag{27}$$

The term $C_2(R)$ is the quadratic Casimir operator of representation R, β is the inverse coupling used on the lattice, and $\langle P\rangle$ is the average plaquette. The Δ values are shown in table 5.

Δ_{Σ_1}	Δ_{γ_μ}	$\Delta_{\gamma_5\gamma_\mu}$
-12.82	-7.75	-3.0

Table 5: The Δ values used in the renormalisation of decay constants.

In order to extrapolate towards the continuum limit, we generate ensembles at several values of the lattice coupling β, and express all physically interesting quantities in units of the gradient flow scale w_0. For each ensemble we consider several bare masses of the valence fermion, restricted to
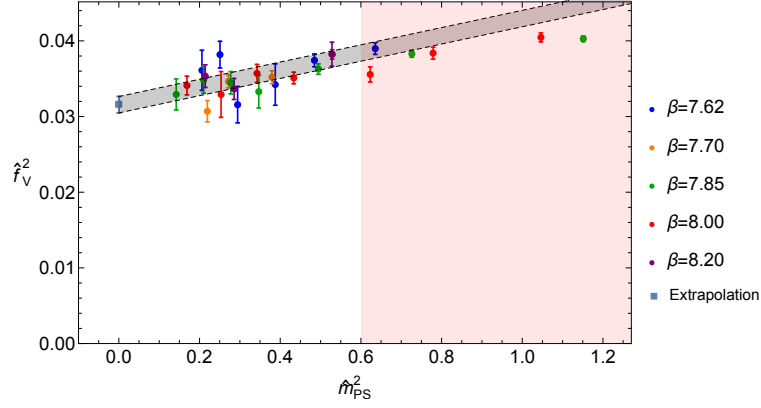
Figure 13: An example of extrapolation to the chiral limit for the vector decay constant for fermions in the fundamental representation of $Sp(4)$. The reduced chi-squared is $\chi^2/N_{\text{dof}} = 1.20$. Data points in the pink shaded region are not included in the curve-fitting procedure. The grey band represents the continuum and massless extrapolation and the vertical width corresponds to the statistical error.
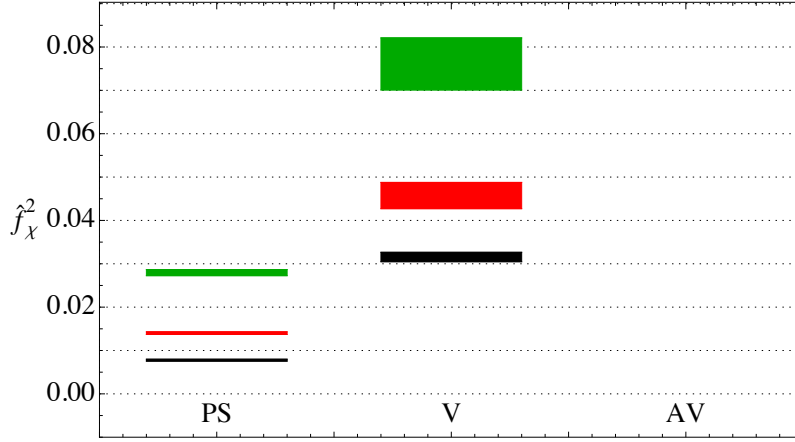

Figure 14: Chiral and continuum extrapolation of the decay constant of mesons with fundamental (black), symmetric (green) and antisymmetric (red) fermions, expressed in units of gradient flow, in $Sp(4)$.

satisfy the following conditions: $am_M \lesssim 1$, $m_{PS}L \gtrsim 7.5$, and $f_{PS}L \gtrsim 1$. Finite volume effects are negligible if the second such condition holds. When the first and third conditions are satisfied, an EFT description exists in which, at the next-to-leading order (NLO), one finds

$$\hat{m}_M^{2,\text{NLO}} = \hat{m}_M^{2,\chi}(1 + L_{m,M}^0 \hat{m}_{PS}^2) + W_{m,M}^0 \hat{a}, \tag{28}$$

$$\hat{f}_M^{2,\text{NLO}} = \hat{f}_M^{2,\chi}(1 + L_{f,M}^0 \hat{m}_{PS}^2) + W_{f,M}^0 \hat{a}. \tag{29}$$

These NLO results display the dependence on the pseudoscalar mass $\hat{m}_{PS}$, which vanishes in the chiral limit. All quantities measured in terms of the gradient-flow are denoted by the caret (ˆ) symbol, e.g. $\hat{f} = f w_0$. The observables in the chiral limit are denoted by the superscript χ. L^0 and W^0 are free parameters to be determined by curve-fitting. An example is shown in Fig. 13.

The results for meson masses and decay constants in the continuum and massless limit for $Sp(4)$ and $Sp(6)$ are shown in Figures 14 to 17—the width of the boxes represents the statistical
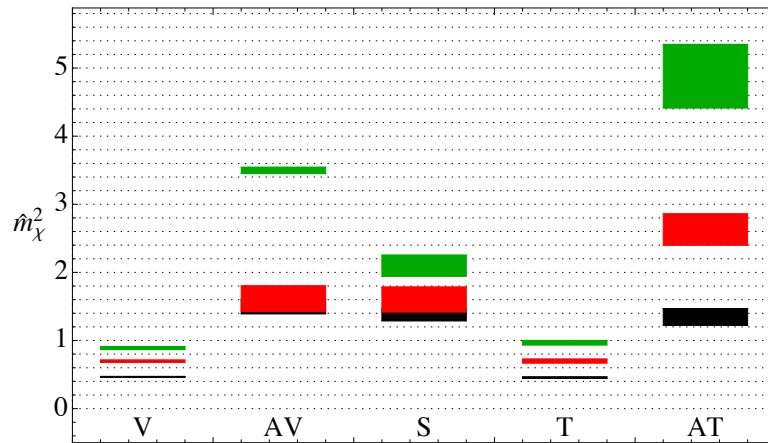
Figure 15: Chiral and continuum extrapolation of the mass squared of mesons with fundamental (black), symmetric (green) and antisymmetric (red) fermions, expressed in units of gradient flow, in $Sp(4)$.
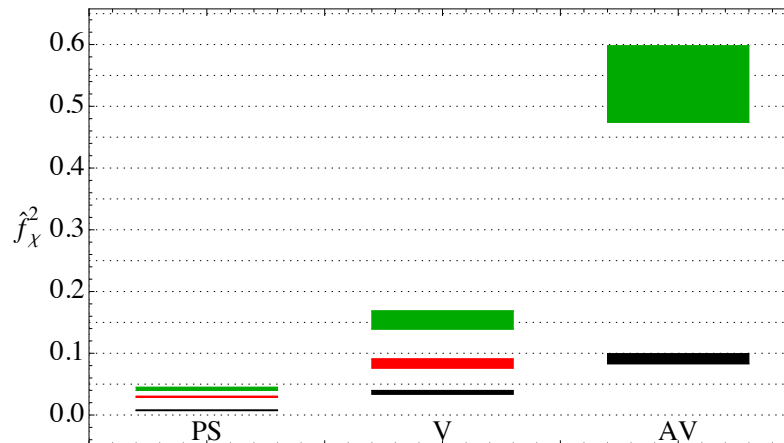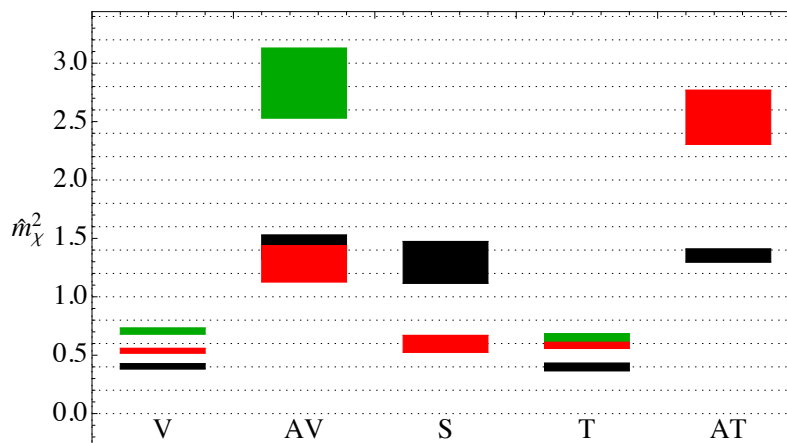

Figure 16: Chiral and continuum extrapolation of the decay constant of mesons with fundamental (black), symmetric (green) and antisymmetric (red) fermions, expressed in units of gradient flow, in $Sp(6)$.

Figure 17: Chiral and continuum extrapolation of the mass squared of mesons with fundamental (black), symmetric (green) and antisymmetric (red) fermions, expressed in units of gradient flow, in $Sp(6)$.

uncertainties. We observe the emergence of a clear hierarchy between the three representations: masses and decay constants tend to increase from fundamental to antisymmetric to symmetric representation. In the cases of $Sp(4)$ with fundamental and antisymmetric valence fermions, the results are comparable with our published results in Ref. [4]. Some of the measurements have been omitted from the plots; this is due to a poor signal in the extrapolation to the chiral limit, signaling an unreliable result. We will provide these results in future publications, which will also report the extrapolation to the large-N limit.

5. Fermions in mixed representations of $Sp(4)$

In this section we return to the CHM candidate proposed in Ref. [17]. It is a $Sp(2N)$ gauge theory with $N_f = 2$ Dirac fermions transforming according to the fundamental representation, and $n_f = 3$ on the 2-index antisymmetric representation. For $N > 1$, mesons made of fundamental representation fermions yield the PNGBs needed for Higgs compositeness, while (partial) top compositeness arises because of the existence of exotic fermionic matter (chimera baryons) composed of two fundamental and one antisymmetric fermion. From now on, we restrict attention to the $Sp(4)$ gauge theory. We discuss some progress we made on the lattice numerical treatment of the theory, and we report preliminary results for the mesons with dynamical antisymmetric fermions, for chimera baryons in the partially quenched theory (in which only the antisymmetric fermions are dynamical) and for the bulk transitions in the fully dynamical theory with mixed representations.

5.1 The lattice theory

The lattice action we adopt contains both fundamental (F) and antisymmetric (AS) fermions:

$$S \equiv S_W + a^4 \sum_{i=1}^{2} \sum_x \overline{Q}_i(x) D^F Q_i(x) + a^4 \sum_{i=1}^{3} \sum_x \overline{\Psi}_i(x) D^{AS} \Psi_i(x), \tag{30}$$

where S_W is the Wilson gauge action in Eq. (3) and D^R is the massive Wilson Dirac operator for fermions in the representation R defined in Eq. (17). We impose periodic boundary conditions in all directions for the gauge fields. For the Dirac fields we consider periodic and antiperiodic boundary conditions for the spatial and temporal extents, respectively. Simulations were carried out using the HiRep code [79] with the standard rational hybrid Monte Carlo (RHMC) algorithms, where several advanced techniques such as even-odd preconditioning can also be accessed. The implementation of $Sp(2N)$ gauge theories with fermions in the fundamental representation is described in Ref. [1]. Details about the antisymmetric representation and for the mixed representation will be discussed in upcoming publications

5.2 Towards composite Higgs and partial top compositeness

With field content comprising $N_f = 2$ fundamental and $n_f = 3$ 2-index antisymmetric fermions, the mass terms break the enhanced global symmetry $SU(4) \times SU(6)$ to the subgroups $Sp(4) \times SO(6)$, which is also the subgroup preserved in the vacuum, in the presence of fermion bilinear condensates. The unbroken generators leave invariant the symplectic matrix Ω and the symmetric matrix ω, which

we write as follows:

$$\Omega = \Omega_{jk} = \Omega^{jk} \equiv \begin{pmatrix} 0 & 0 & 1 & 0 \\ 0 & 0 & 0 & 1 \\ -1 & 0 & 0 & 0 \\ 0 & -1 & 0 & 0 \end{pmatrix}, \quad \omega = \omega_{jk} = \omega^{jk} \equiv \begin{pmatrix} 0 & 0 & 0 & 1 & 0 & 0 \\ 0 & 0 & 0 & 0 & 1 & 0 \\ 0 & 0 & 0 & 0 & 0 & 1 \\ 1 & 0 & 0 & 0 & 0 & 0 \\ 0 & 1 & 0 & 0 & 0 & 0 \\ 0 & 0 & 1 & 0 & 0 & 0 \end{pmatrix}. \tag{31}$$

We decompose the antisymmetric representation of $Sp(4)$ as $5 = 4 + 1$ of $SO(4)$, and we identify the gauged $SU(2)_L$ of the SM, and its approximate $SU(2)_R$, as $SU(2)_L \times SU(2)_R \sim SO(4) \subset Sp(4)$. By doing so, the complex scalar doublet of $SU(2)_L$ is identified with the 4 of $SO(4)$. The corresponding operators are flavoured mesons (and diquarks) built of fundamental fermions.

The chimera baryons that have the same quantum numbers of the top quark can mix with it, providing an origin for its mass (partial top compositeness). Such quantum numbers can be obtained by combining the 4 of $SO(4)$ with the antisymmetric fermions Ψ^k. Since the $SU(3) \times SU(3)$ subgroup of $SU(6)$ breaks into $SU(3)_V$, it is natural to identify the QCD gauge group as $SU(3)_c \sim SU(3)_V \subset SO(6)$, and write the following fermion operators:

$$\begin{aligned} O_{\text{CB},1} &= \left(\overline{Q^{1\,a}} \gamma^5 Q^{2\,b} + \overline{Q^{2\,a}} \gamma^5 Q^{1\,b} \right) \Omega_{bc} \Psi^{k\,ca}, \\ O_{\text{CB},2} &= \left(-i \overline{Q^{1\,a}} \gamma^5 Q^{2\,b} + i \overline{Q^{2\,a}} \gamma^5 Q^{1\,b} \right) \Omega_{bc} \Psi^{k\,ca}, \\ O_{\text{CB},4} &= -i \left(\overline{Q^{1\,a}} Q_C^{2\,b} + \overline{Q_C^{2\,a}} Q^{1\,b} \right) \Omega_{bc} \Psi^{k\,ca}, \\ O_{\text{CB},5} &= i \left(-i \overline{Q^{1\,a}} Q_C^{2\,b} + i \overline{Q_C^{2\,a}} Q^{1\,b} \right) \Omega_{bc} \Psi^{k\,ca}. \end{aligned} \tag{32}$$

The $U(1)_A$ partners can be obtained by replacing $\mathbb{1}_4 \rightarrow i\gamma^5$ in the fundamental bilinears. For completeness, the $SO(4)$ singlet that combines with the 4 into the 5 of $SO(5)$ is

$$O_{\text{CB},3} = \left(\overline{Q^{1\,a}} \gamma^5 Q^{1\,b} - \overline{Q^{2\,a}} \gamma^5 Q^{2\,b} \right) \Omega_{bc} \Psi^{k\,ca},$$

and plays no role in top compositeness.

To construct the interpolating operators on the lattice, we start from the most generic gauge-invariant fermion composite of two fundamental fermions and one antisymmetric fermion:

$$O_{\text{CB}}^\alpha(x) = D^{\alpha\beta\gamma\delta} \Omega_{ac} \Omega_{bd} Q_\beta^{i\,a}(x) Q_\gamma^{j\,b}(x) \Psi_\delta^{k\,cd}(x). \tag{33}$$

We use Greek letters to denote for the spin indices, to distinguish them from the colour and flavour indices. The simplest operator interpolating the spin-$1/2$ ground state would be analogous to the Λ-baryon in QCD, which is $D^{\alpha\beta\gamma\delta} = -i(\gamma^5 C)^{\beta\gamma} \delta^{\alpha\delta}$ with $C = i\gamma^2\gamma^0$ being the charge conjugation matrix.[2] The 4 of $SO(4)$ and 3 of $SU(3)_V$ are identified by appropriate choices of i, $j = 1$, 2 with $i \neq j$, and $k = 1$, 2, 3. We perform the parity projection in the nonrelativistic limit,

$$O_{\text{CB}}^\pm(x) \equiv \mathcal{P}_\pm O_{\text{CB}}(x), \quad \text{with } \mathcal{P}_\pm = \frac{1}{2} \left(1 \pm \gamma_0 \right). \tag{34}$$

---

[2] The other common choice of the Dirac structure would be $D^{\alpha\beta\gamma\delta} = -i(C)^{\beta\gamma}(\gamma^5)^{\alpha\delta}$.
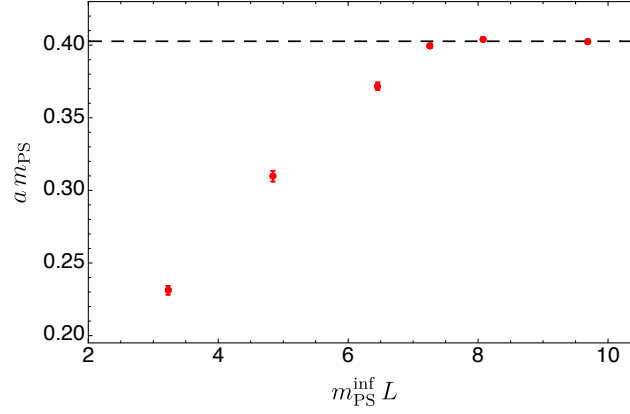
Figure 18: Pseudoscalar meson mass am_{PS} (in lattice units) versus $m_{\mathrm{PS}}L$, where L is the extension of a spatial direction, for varying L/a and fixed $T/a = 54$, with $\beta = 6.8$ and $m_0 = -1.03$. The horizontal line is the measurement at the largest volume of 54×24^3, taken to represent the infinite volume extrapolation.

Using the interpolating operator in Eq. (34) and its conjugate, we construct the propagator for the Chimera baryon at positive Euclidean time t and vanishing momentum $\vec{p}$

$$
\begin{aligned}
\langle O_{\mathrm{CB}}^{\pm}(t)\overline{O_{\mathrm{CB}}^{\pm}(0)}\rangle &= \sum_{\vec{x}} \Omega_{da}\Omega_{bc}\Omega^{c'b'}\Omega^{a'd'} S_{\Psi}(t,\vec{x})_{\alpha,\alpha'}^{ca,c'a'}(t,\vec{x})\mathcal{P}_{\pm}^{\alpha',\alpha} \\
&\times S_Q^j(t,\vec{x})_{\gamma,\gamma'}^{d,b'}(t,\vec{x})(C\gamma^5)_{\gamma\beta}S_Q^i(t,\vec{x})_{\beta,\beta'}^{b,d'}(t,\vec{x})(C\gamma^5)_{\gamma'\beta'},
\end{aligned}
\tag{35}
$$

where the fermion propagators are

$$
S_Q(t,\vec{x})_{\alpha,\beta}^{a,b} = \langle Q(t,\vec{x})_\alpha^a \overline{Q(0)^b}_\beta\rangle \text{ and } S_\Psi(t,\vec{x})_{\alpha,\beta}^{ab,cd} = \langle \Psi(t,\vec{x})_\alpha^{ab}\overline{\Psi(0)^{cd}}_\beta\rangle.
\tag{36}
$$

5.3 Mesons with $n_f = 3$ dynamical antisymmetric Dirac fermions

We turn now our attention to the spectroscopy study of the $Sp(4)$ gauge theory with $n_f = 3$ dynamical Dirac fermions on the antisymmetric representation. We measure the masses of the ground-state mesons using the operators listed in table 4. For the meson analogous to the ρ in QCD, the physical states have overlap with two different operators O_V and O_T, hence we also implement the generalised eigenvalue problem [82], to extract the mass of the excited state (analogous to the ρ' in QCD). In our preliminary studies of the bare parameter space via the mass scan [2], we found a first-order bulk phase transition at strong coupling and determined the lower bound in the lattice coupling for the weak coupling regime as $\beta \gtrsim 6.6$.

We start by studying finite size effects. In Fig 18, we present the pseudoscalar mass in lattice units measured at six different lattice volumes with isotropic spatial extents $L/a = 8, 12, 16, 18, 20, 24$ and common temporal extent $T/a = 54$. We find that the mass of pseudoscalar mesons converges for $m_{\mathrm{ps}}L \gtrsim 8$, indicating that finite volume effects are negligible for $m_{\mathrm{ps}} \gtrsim 8$. All the measurements reported in the following satisfy this condition.

Finite volume effect results in a negative contribution to the pseudoscalar mass, which is the opposite to the typical lattice QCD results. In fact, such a distinct behavior can be understood in the context of chiral perturbation theory (χPT). Finite volume corrections are accounted for by loops
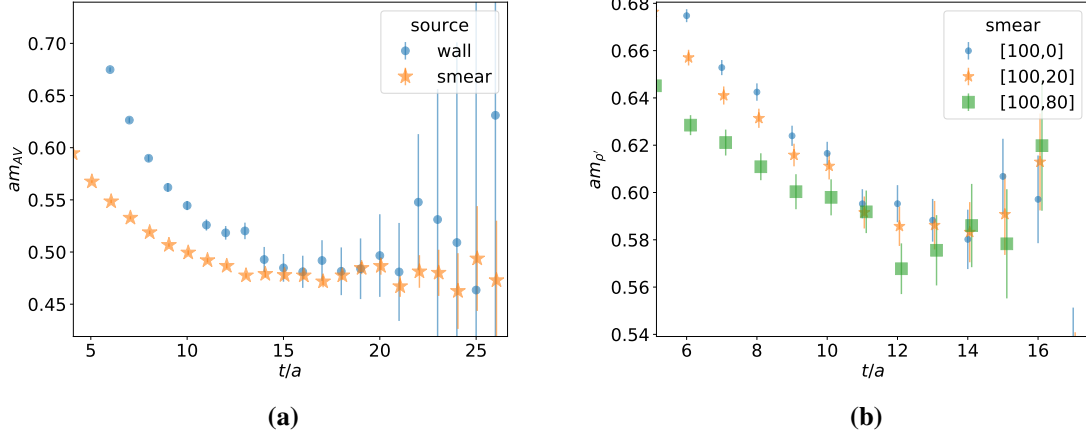
(a)   **(b)**

Figure 19: **(a)** Comparison of axial-vector meson effective mass plot with Z_2-wall source and smeared source. The number of iterations at the sink for axial vector meson is tuned to optimise signal. **(b)** Effective mass plot of excited ρ meson at different levels of sink smearing. The smearing parameters are $\varepsilon = 0.16$ and $N_W = 100$ at the source, while $N_W = 0, 20, 80$ for the sink—values in the square bracket in the legend. Both panels present calculations performed on a 54×32^3 lattice, with $\beta = 6.8$ and $m_0 = -1.04$.

wrapping around each spatial extent of the lattice, and the resulting summations at finite volume modify the pseudoscalar mass. At the next-to-leading order (NLO), one has

$$m_{\rm PS}^2 = M^2 \left(1 + a_M \frac{A(M) + A_{\rm FV}(M)}{F^2} + b_M(\mu)\frac{M^2}{F^2} + O(M^4)\right), \tag{37}$$

with

$$A(M) = -\frac{M^2}{16\pi^2}\log\frac{M^2}{\mu^2} \text{ and } A_{\rm FV}(M) \stackrel{ML \gg 1}{\longrightarrow} -\frac{3}{4\pi^2}\left(\frac{M\pi}{2L^3}\right)^{1/2}\exp[-ML], \tag{38}$$

where M and F are the pseudoscalar mass and decay constant (at leading order) and μ is the renormalisation scale. The result $A_{\rm FV}(M)$ for the finite sum has been obtained from a cubic box of size L with periodic boundary condition (see the Appendix of Ref. [83]), and is independent of the details of the theory. But, the coefficient a_M reflects the symmetry breaking pattern [84]:

$$a_M = \begin{cases} \frac{1}{2} - \frac{1}{2n_f}, & \text{for } SU(2N_f) \to SO(2N_f), \\ -\frac{1}{n_f}, & \text{for } SU(N_f) \times SU(N_f) \to SU(N_f), \\ -\frac{1}{2} - \frac{1}{n_f}, & \text{for } SU(2N_f) \to Sp(2N_f). \end{cases} \tag{39}$$

The theory with $n_f = 3$ belongs to the first class, and has different sign compared to the other two cases. The analytical results in Eqs. (37), (38) and (39) are hence consistent with the negative corrections displayed in Fig. 18.

In our previous studies [1, 3, 4], we used stochastic Z_2-wall sources to calculate correlation functions [85]. Unfortunately, as we can see in Fig 19a, the effective mass of the axial-vector mesons is noisy at large euclidean time. It is even harder to extract the mass of excited rho using the wall source. To overcome this difficulty, we employ the well-known lattice technique dubbed
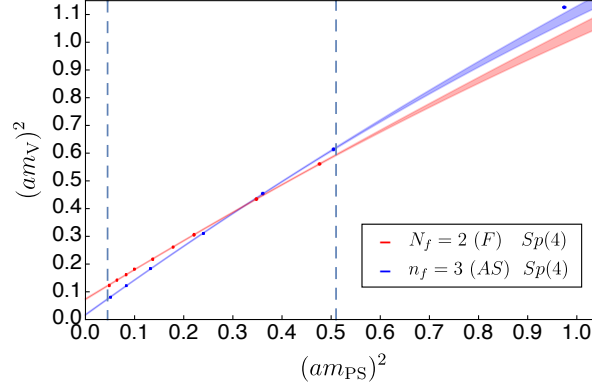
23

Figure 20: Comparison of the massless extrapolations of the vector meson masses, obtained with $\beta = 7.2$ with fundamental fermions, and $\beta = 6.7$ with antisymmetric fermions. The vertical dash lines demarcate the fit range.

Wuppertal smearing [86], to improve signals. The smearing function is defined as follows:

$$q^{(n+1)}(x) = \frac{1}{1 + 6\varepsilon} \left[q^{(n)}(x) + \varepsilon \sum_{\mu=\pm 1}^{\pm 3} U_\mu(x) q^{(n)}(x + \hat{\mu}) \right] \tag{40}$$

where $q^{(0)}(x) = \delta(x)$ and $q^{(n)}$, with $n = 0, \cdots, N_W$ are the smeared source resulting from an iterative process. The tunable parameters ε and N_W are step size and number of iterations respectively. We supplement the source smearing by smoothening the gauge links with APE smearing [87]:

$$U_\mu^{(n+1)}(x) = P \left\{ (1 - \alpha) U_\mu^{(n)}(x) + \frac{\alpha}{6} S_\mu^{(n)}(x) \right\}, \tag{41}$$

with $n = 0, \cdots, N_{APE}$ where we smeared link is

$$S_\mu(x) = \sum_{\pm \nu \neq \mu} U_\nu(x) U_\mu(x + \hat{\nu}) U_\nu^\dagger(x + \hat{\mu}).$$

This process removes short-distance fluctuations of the gauge fields. The effective mass is sensitive to the parameters ε and N_W of the Wuppertal smearing, which need to be optimised. The effect of APE smearing on the effective mass is less dramatic, as long as the smeared spacial plaquette is close to 1. We take $\alpha = 0.4$ and $N_{APE} = 50$, for all ensembles in this study.

Fig. 19a shows that the effective mass after smearing displays the earlier appearance of a longer plateau, and smaller errors. We arrived at optimal smearing by tuning the number of iterations at the sink while fixing the number at the source. If we could not obtain the desired plateau, we would change the smearing level at the source. Fig. 19b illustrates the effect of different levels of sink smearing. The adoption of a multi-source strategy further improves statistical precision.

One noticeable finding of our study is that it is more difficult to decrease the ratio m_{ps}/m_v with antisymmetric matter compared to fundamental fermions. We find $m_{ps}/m_v \simeq 0.8$ for parameter choices giving the lightest pseudoscalar meson mass. To generate ensembles with lighter pseudoscalar meson mass, we would require larger lattices, to suppress finite size effects, hence
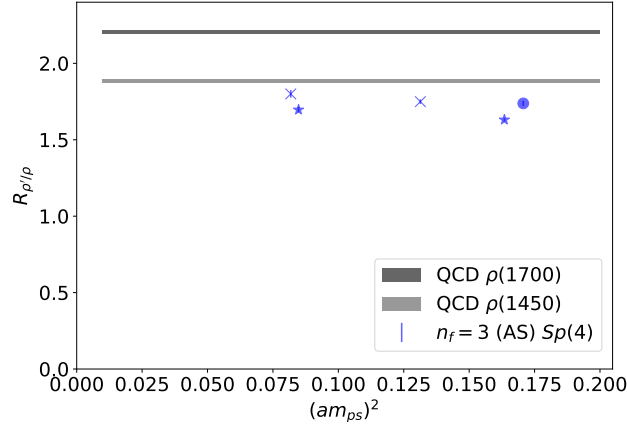
Figure 21: The mass ratio $R_{\rho'/\rho}$ of excited vectors states to the ground state for varying (am^2_{PS}). The blue dots are our calculations in antisymmetric representation. The circle, x-shaped dot and star refer to different choices of $\beta = 6.65$, 6.7, and 6.8, respectively. The grey bands denote the experimental value in QCD [88].
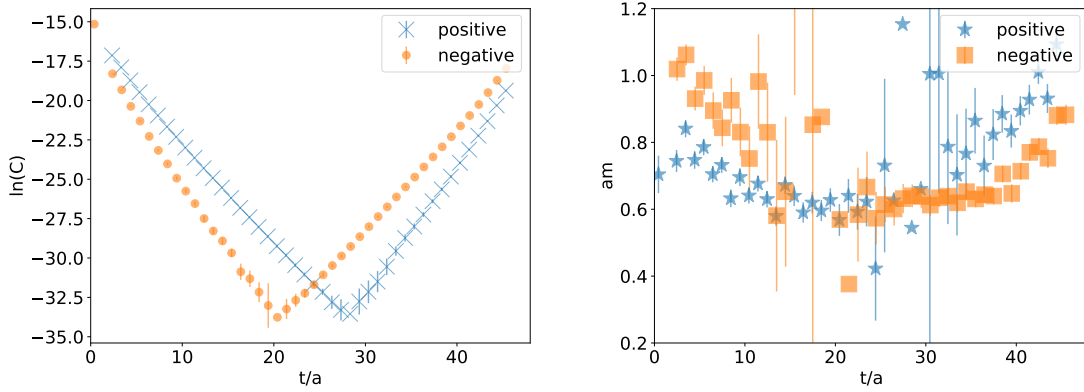

Figure 22: The log plot of the chimera baryon correlators (left panel) and their effective mass plot (right panel) with the parity projections.

increasing the demand for computation resources. Fig. 20 shows a comparison of the mass dependence of the vector meson mass squared with our earlier work on the theory with fundamental matter [3], at fixed lattice couplings. We find that the antisymmetric case approaches the massless limit with a sharper slope and a tiny chiral value of $(am^\chi_V)^2$. This phenomenon might be an early indication that the theory with fermions in the antisymmetric representation is closer to the conformal window, and thus deserves further exploration, by extending the measurements to a larger set of ensembles.

Another interesting preliminary result pertains to the ratio of masses of excited vector mesons to the ground state. Fig. 21 shows that this ratio is about 1.7 in the antisymmetric representation. This is slightly lower than in QCD [88]. Yet, direct comparison is not possible, as we have not yet performed the continuum extrapolation.

As a first step towards studying the spectrum of chimera baryons, we use these same ensembles,
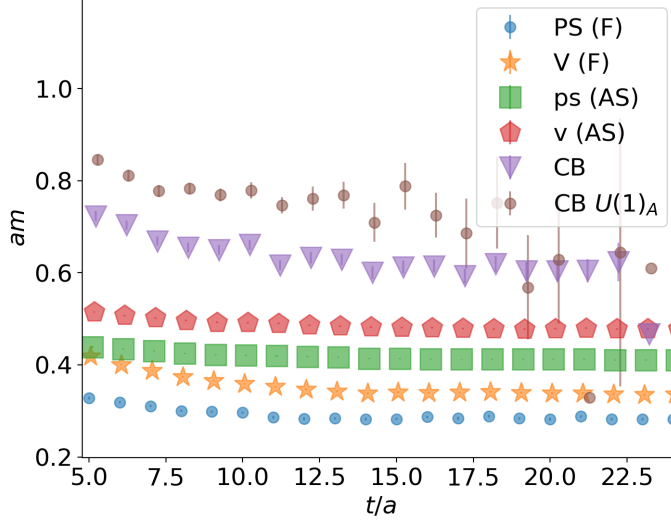
Figure 23: Effective masses plot measured from 48×24^3 lattice with $\beta = 6.65$ and $m_0 = -1.07$ using dynamical antisymmetric fermions. The quenched fundamental bare mass is $m_{\mathrm{f}} = -0.734$. The blue and orange are pseudoscalar and vector mesons with quenched fundamental fermions. The green and red are pseudoscalar and vector mesons with dynamical antisymmetric fermions. The purple and brown are chimera baryons and their $U(1)_A$ partner.

partially quenching the theory by treating the $N_f = 2$ fundamental fermions as non-dynamical—we expect the $n_f = 3$ antisymmetric fermions to have a stronger effect on the dynamics. To enable a comparison, we tune the valence fundamental-fermion masses such that $m_{\mathrm{PS}}/m_{\mathrm{V}} \sim m_{\mathrm{ps}}/m_{\mathrm{v}}$—the former being the mass ratio for the mesons made of quenched fundamental fermions, the latter measured with dynamical antisymmetric ones. The effective mass of the chimera baryons defined in Eq. (35) is presented in Fig. 22, after parity projection with $P_{\pm} = (1 \pm \gamma_0)$. The correlation functions exhibit an asymmetric behaviour: the backward propagator with a given parity agrees with the forward propagator with the opposite parity, as is the case for nucleons in lattice QCD [89]. A comparison of the effective mass of chimera baryons and mesons is displayed in Fig 23.

5.4 Dynamical studies with $N_f = 2$ fundamental and $n_f = 3$ antisymmetric Dirac fermions

We modified the HiRep code [79] to perform dynamical calculations with both fermions in the fundamental and antisymmetric representation, with the matter content require by the CHM in Ref. [17], and we have been carrying on an extensive programme of testing of the resulting numerical algorithms. Besides the volume, the lattice theory depends on three couplings: β and the masses of fermions in the fundamental and antisymmetric representations, denoted as m_0^{f} and m_0^{as}, respectively. We hence explored the parameter space to identify the phase transitions.

Fig. 24 displays a three-dimensional cartoon of the phase space of the $Sp(4)$ theory with mixed representation. The black surface denotes the first order phase transition. The three (coloured) lines correspond to the first order lines at fixed representative choices of β. For small β (red line) a phase transition occurs for all the possible fermions masses. With moderate β (blue lines), the
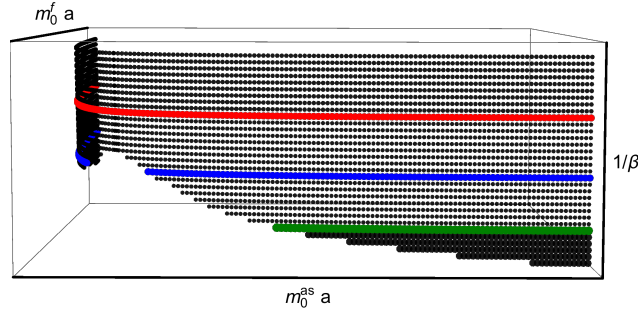
Figure 24: Cartoon of the phase space for the *Sp*(4) gauge theory coupled to fermions in both fundamental (F) and antisymmetric (AS) representations, as a functions of the lattice parameters β, m_0^{f}, and m_0^{as}. A first order bulk phase transition takes place on a surface with boundaries inside the three-dimensional space.

phase transition disappears when both fermions are light, and the line of phase transitions has an end point. The boundary of the first order surface is asymmetric, and for even larger β the phase transition depends only on the mass of the antisymmetric fermions. We reported elsewhere that the asymptotic values of the critical coupling in the quenched limit of either the fundamental antisymmetric fermions are different, with $\beta_{\mathrm{cr}}^{\mathrm{f}} \sim 6.7$ [1] and $\beta_{\mathrm{cr}}^{\mathrm{as}} \sim 6.5$ [2].

In Fig. 25, we fix $\beta = 6.4$, to match with the blue line in Fig. 24, and show the value of the average plaquette for four representative choices of phase-space trajectories that cross the blue lines at points A, B, C, D. In three cases, we find strong evidence of hysteresis, indicating the presence of a first-order phase transition, while for C the absence of hysteresis suggests that the theory is in a cross-over region. These results are consistent with earlier evidence that the theories with fermions in either representation show a first-order transition at $\beta = 6.4$ [1, 2].

Fig. 26 illustrates our strategy to identify a critical value of β, corresponding to the end of the first order surface, at given values of the bare mass parameters. We fix the mass $am_0^{\mathrm{f}} = -0.6$, of the fundamental fermions and compute the difference of the average plaquette values between cold and hot starts, for varying choices of β. The left panel of the figure shows that $\langle\Box\rangle_{\mathrm{cold}} - \langle\Box\rangle_{\mathrm{hot}}$ is nonzero for $\beta \lesssim 6.3$, but is consistent with zero for $\beta = 6.4$. In the right panel, we show that having fixed $\beta = 6.4$, by computing the plaquette susceptibility χ_{plaq} we find that its peak is independent of the volume, consistently with a crossover. We hence led to conclude that for $\beta \gtrsim 6.4$ the mixed-representation theory is in the weak-coupling regime.

We next turn our attention to finite size effects. We start by fixing $\beta = 6.5$, $am_0^{\mathrm{f}} = -0.71$, and $am_0^{\mathrm{as}} = -1.01$, and we vary the volume. In the left panel of Fig. 27, we show the average plaquette measured on lattice volumes varying from 36×8^3 to 48×24^3, in terms of $m_{\mathrm{PS}}^{\mathrm{inf}} L$, the mass of pseudoscalar meson with constituents given by the fermions in the fundamental representation— the lightest state in the spectrum–in units of the lattice size. $am_{\mathrm{PS}}^{\mathrm{inf}}$ denotes the mass measured at the largest available volume. Finite volume correction to the plaquette are no larger than a per mile effect, and are negligible for $m_{\mathrm{PS}}^{\mathrm{inf}} L \gtrsim 6.5$.

In the right panel of the figure, we present the masses of the pseudoscalar mesons composed of constituent fermions in the fundamental and antisymmetric representations, measured in different volumes. Finite volume corrections are at the percent level and comparable to the statistical errors
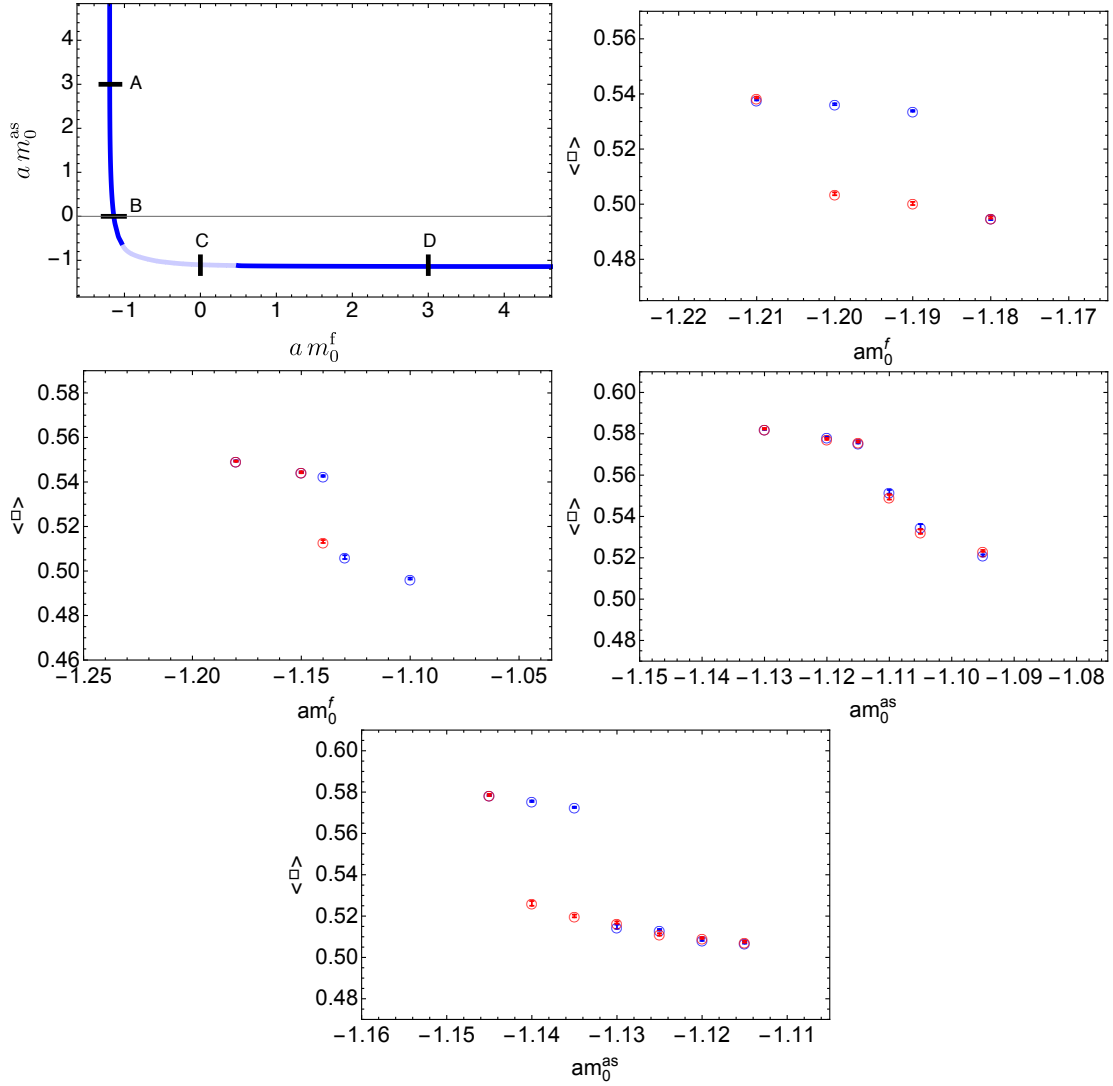
Figure 25: The top-left panel displays a section at fixed $\beta = 6.4$ of the phase structure of the two-representation $Sp(4)$ theory from Fig. 24. The (blue) solid line denotes the first order phase transition, while the light blue line denotes a crossover. From top-right to bottom, the other four panels show the average plaquette values, which are extracted for the calculations with initial configuration given by unit (blue) or random (red) matrices, for parameter choices adjusted to cross the phase boundaries at the points A, B, C and D in the top-left panel. Numerical results are obtained from the lattice volume of 8^4.

when $m_{\mathrm{PS}}^{\inf} L \gtrsim 7$. Preliminary analyses not reported here confirm that finite size corrections to the masses of chimera baryons and other mesons in other channels, and to the pseudocalar decay constant, are negligible under the same condition to the lattice volume. As observed earlier, finite volume corrections to the pseudoscalar mass have opposite signs depending on the constituent fermions, consistently with the predictions of chiral perturbation theory at finite volume.

We performed the first calculations of the spectrum of chimera baryons in the $Sp(4)$ theory with mixed-representation dynamical matter fields ($N_f = 2$ and $n_f = 3$), and carried out several
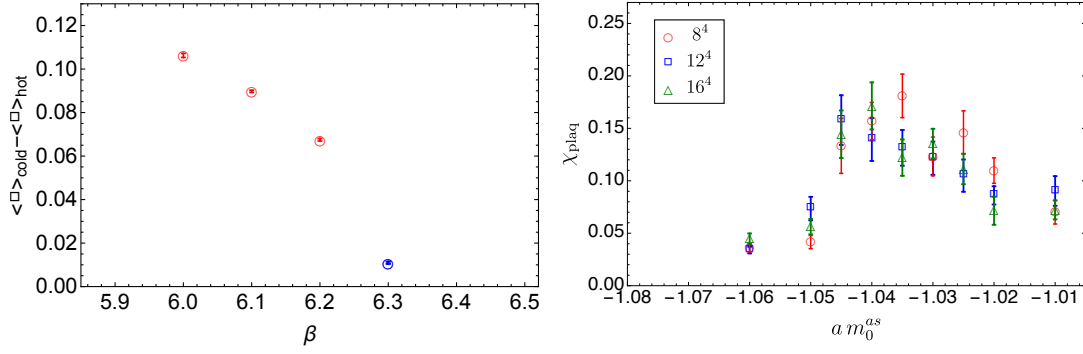
Figure 26: Left panel: the difference of the average plaquette values between cold (unit) and hot (random) initial configurations, at fixed bare mass $am_0^f = -0.6$ for the fundamental fermion. Red and blue symbols refer to lattice volumes of 8^4 and 12^4, respectively. Right panel: plaquette susceptibilities at fixed coupling $\beta = 6.4$ and bare mass of $am_0^f = -0.6$, for several different volumes.
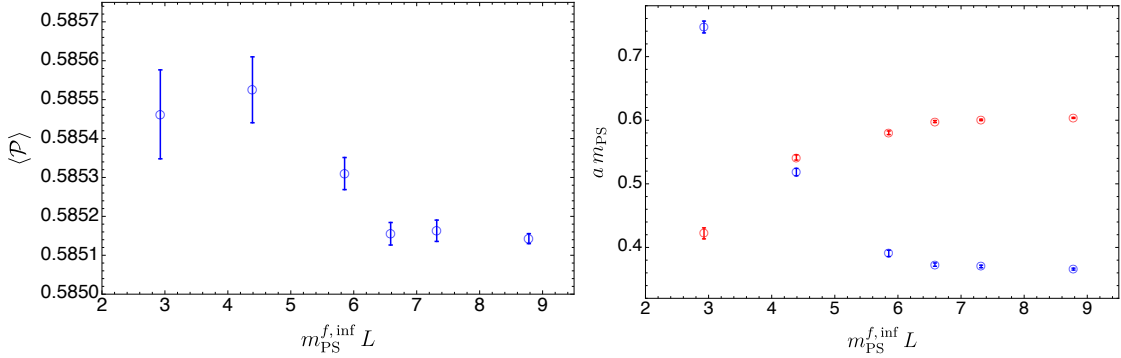

Figure 27: Finite volume effects displayed by the average plaquette (left panel) and the mass of pseudoscalar mesons (right panel) in which the constituent fermions are in the fundamental (blue) and antisymmetric (red) representations, for $\beta = 6.5$, $am_0^f = -0.71$, $am_f^{as} = -1.01$.

non-trivial tests. The upper panels of Fig. 28 display the real and imaginary parts of the correlation function. While the former shows a clear signal of exponential decay, and a beautiful symmetry between forward and backward propagation, statistical fluctuations in the latter are larger than the signal. The lower panels of Fig. 28 are obtained by computing the real and imaginary parts of the correlators after acting with the parity projector onto the baryon interpolating operators. In this case, the real part $C_{re}(\tau)$ is asymmetric in respect to Euclidean time: the forward and backward propagators correspond to the even and odd parity states, respectively. The imaginary part is again just statistical noise, but after parity projection the fluctuations of the imaginary part are now about ten orders of magnitude smaller than the error on the real part.

We conclude with an illustrative example of the spectrum obtained for fixed lattice parameters in Fig. 29. We present the masses of flavoured spin−0 and spin−1 mesons with the constituents either in the fundamental or in the antisymmetric representation, as well as the mass of the parity-even chimera baryon. With these choices of lattice parameters, the mesons composed of fundamental-
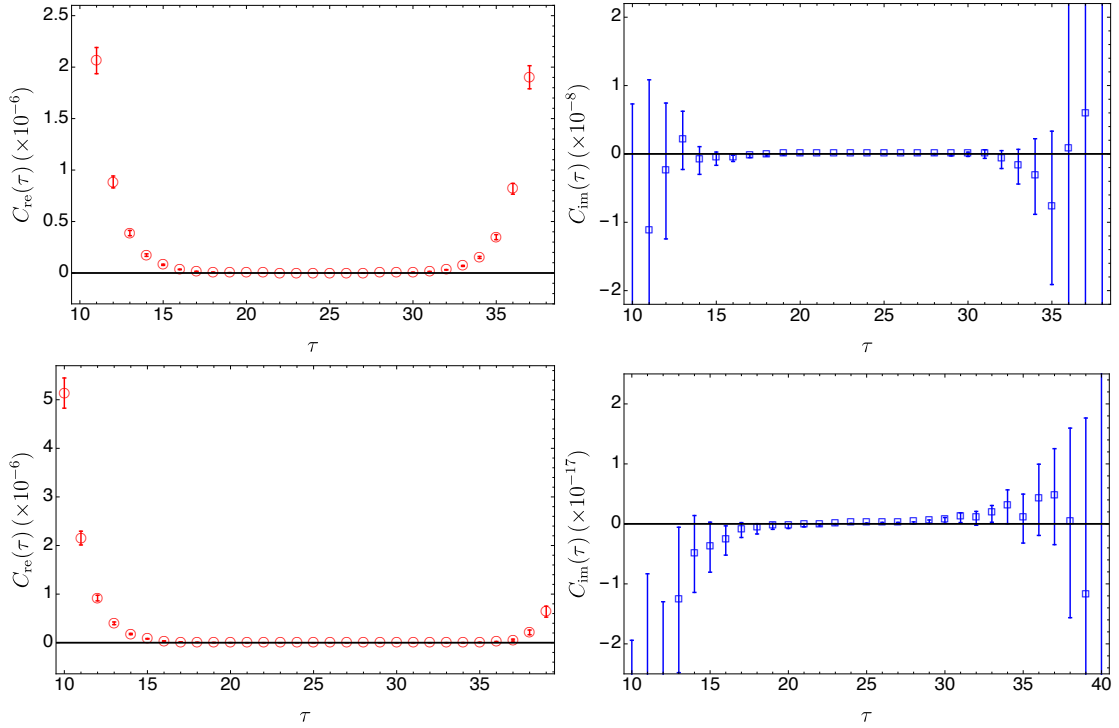
Figure 28: Real and imaginary parts of the two-point Euclidean correlation function of chimera baryons in the dynamical mixed-representation theory, before (upper panels) and after (bottom panels) parity projection. The lattice parameters are $\beta = 6.5$, $am_0^{\mathrm{f}} = -0.71$, $am_f^{\mathrm{as}} = -1.01$, and the lattice volume is 48×24^3.

representation constituents are much lighter than those of antisymmetric-representation ones, yet the mass difference is approximately independent of the meson. The lightest chimera baryon has mass similar to the scalar meson composed of antisymmetric-representation fermions.

6. Outlook

We summarised preliminary results for an extensive programme of explorations on the lattice of gauge theories with $Sp(2N)$ group. We will follow up this Proceedings contribution with a series of publications reporting more extensive studies, and definite physics results, yet these preliminary measurements illustrate our processes and our current stage of progress in the programme.

In the case of the pure Yang-Mills theories, we will collect a larger number of ensembles, perform the continuum limit extrapolations of the $Sp(2N)$ topological susceptibility for $N = 1, 2, 3, 4$, extrapolate to $N \rightarrow +\infty$, and compare to available literature on the $SU(N_c)$ theories, possibly by using the string tension σ as a physical comparison scale.

We will complete the extensive programme of computing the spectrum of mesons in the fundamental, as well as 2-index symmetric and antisymmetric representations, in the quenched approximation, by extending it to the $N = 4$ case, performing combined continuum and chiral extrapolations, and combining the results for $N = 1, 2, 3, 4$ towards approaching the large-N limit.
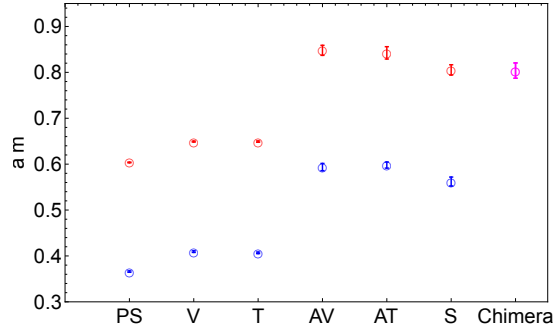
Figure 29: Illustrative example of mass spectrum of composite states in the mixed-representation dynamical $Sp(4)$ theory. The lattice parameters are $\beta = 6.5$, $am_0^{as} = -1.01$, $am_0^f = -0.71$, and the lattice volume is 48×24^3. Blue and red symbols denote flavoured mesons composed of the fundamental and antisymmetric representation constituents, respectively, in different channels—pseudoscalar (PS), vector (V), tensor (T), axial vector (AV), axial tensor (AT), and scalar (S). The magenta symbol denotes the chimera baryon with $J^P = \frac{1}{2}^+$, with interpolating operator consisting of one antisymmetric and two fundamental fermions.

For dynamical fermions in the antisymmetric representation of $Sp(4)$, we saw that the approach to the chiral limit is slow, and hence we will study a larger number of ensembles, moving closer both towards lower mass, and towards the continuum. We will study the extrapolations to the continuum limit for the spectrum of mesons, and include also some of the excited states in the spectrum. A systematic study of the spectrum of partially quenched chimera baryons composed of one fermion in the 2-index antisymmetric and two (quenched) in the fundamental representation is under way.

For the fully dynamical $Sp(4)$ theory with mixed-representation fermions, for which we chose the field content to match the CHM in Ref. [17], our next step requires completing an extensive study of the general properties of the lattice theory, reaching beyond the scan of parameter space presented here. We will then be in a position to start performing systematic studies of the spectrum of the theory that are relevant both to composite Higgs and partial top compositeness.

The completion and combination of the aforementioned measurements has potential transformative effect on the current understanding of $Sp(2N)$ gauge theories, providing unprecedented level of quantitative information about them. Besides the specific application to the CHM we investigate, this information can be used as a starting point for the characterisation of other CHMs, or models of dark matter with strong-coupling origin, and might have applications in other fields of study.

Acknowledgments

References

[1] E. Bennett, D. K. Hong, J. W. Lee, C.-J. D. Lin, B. Lucini, M. Piai and D. Vadacchino, "Sp(4) gauge theory on the lattice: towards SU(4)/Sp(4) composite Higgs (and beyond)," JHEP **1803**, 185 (2018) doi:10.1007/JHEP03(2018)185 [arXiv:1712.04220 [hep-lat]].

[2] J. W. Lee, E. Bennett, D. K. Hong, C. J. D. Lin, B. Lucini, M. Piai and D. Vadacchino, "Progress in the lattice simulations of Sp(2N) gauge theories," PoS LATTICE **2018**, 192 (2018) doi:10.22323/1.334.0192 [arXiv:1811.00276 [hep-lat]].

[3] E. Bennett, D. K. Hong, J. W. Lee, C. J. D. Lin, B. Lucini, M. Piai and D. Vadacchino, "Sp(4) gauge theories on the lattice: $N_f = 2$ dynamical fundamental fermions," JHEP **12**, 053 (2019) doi:10.1007/JHEP12(2019)053 [arXiv:1909.12662 [hep-lat]].

[4] E. Bennett, D. K. Hong, J. W. Lee, C. J. D. Lin, B. Lucini, M. Mesiti, M. Piai, J. Rantaharju and D. Vadacchino, "*Sp*(4) gauge theories on the lattice: quenched fundamental and antisymmetric fermions," Phys. Rev. D **101**, no.7, 074516 (2020) doi:10.1103/PhysRevD.101.074516 [arXiv:1912.06505 [hep-lat]].

[5] E. Bennett, J. Holligan, D. K. Hong, J. W. Lee, C. J. D. Lin, B. Lucini, M. Piai and D. Vadacchino, "Color dependence of tensor and scalar glueball masses in Yang-

Mills theories," Phys. Rev. D **102**, no.1, 011501 (2020) doi:10.1103/PhysRevD.102.011501 [arXiv:2004.11063 [hep-lat]].

[6] E. Bennett, J. Holligan, D. K. Hong, J. W. Lee, C. J. D. Lin, B. Lucini, M. Piai and D. Vadacchino, "Glueballs and strings in *Sp*(2*N*) Yang-Mills theories," Phys. Rev. D **103**, no.5, 054509 (2021) doi:10.1103/PhysRevD.103.054509 [arXiv:2010.15781 [hep-lat]].

[7] K. Holland, M. Pepe and U. J. Wiese, "The Deconfinement phase transition of Sp(2) and Sp(3) Yang-Mills theories in (2+1)-dimensions and (3+1)-dimensions," Nucl. Phys. B **694**, 35-58 (2004) doi:10.1016/j.nuclphysb.2004.06.026 [arXiv:hep-lat/0312022 [hep-lat]].

[8] D. B. Kaplan and H. Georgi, "SU(2) x U(1) Breaking by Vacuum Misalignment," Phys. Lett. B **136**, 183-186 (1984) doi:10.1016/0370-2693(84)91177-8

[9] H. Georgi and D. B. Kaplan, "Composite Higgs and Custodial SU(2)," Phys. Lett. **145B**, 216 (1984). doi:10.1016/0370-2693(84)90341-1

[10] M. J. Dugan, H. Georgi and D. B. Kaplan, "Anatomy of a Composite Higgs Model," Nucl. Phys. B **254**, 299 (1985). doi:10.1016/0550-3213(85)90221-4

[11] G. Panico and A. Wulzer, "The Composite Nambu-Goldstone Higgs," Lect. Notes Phys. **913**, pp.1 (2016) doi:10.1007/978-3-319-22617-0 [arXiv:1506.01961 [hep-ph]].

[12] O. Witzel, "Review on Composite Higgs Models," PoS LATTICE **2018**, 006 (2019) doi:10.22323/1.334.0006 [arXiv:1901.08216 [hep-lat]].

[13] G. Cacciapaglia, C. Pica and F. Sannino, "Fundamental Composite Dynamics: A Review," Phys. Rept. **877**, 1-70 (2020) doi:10.1016/j.physrep.2020.07.002 [arXiv:2002.04914 [hep-ph]].

[14] G. Ferretti and D. Karateev, "Fermionic UV completions of Composite Higgs models," JHEP **03**, 077 (2014) doi:10.1007/JHEP03(2014)077 [arXiv:1312.5330 [hep-ph]].

[15] G. Ferretti, "Gauge theories of Partial Compositeness: Scenarios for Run-II of the LHC," JHEP **06**, 107 (2016) doi:10.1007/JHEP06(2016)107 [arXiv:1604.06467 [hep-ph]].

[16] G. Cacciapaglia, G. Ferretti, T. Flacke and H. Serôdio, "Light scalars in composite Higgs models," Front. Phys. **7**, 22 (2019) doi:10.3389/fphy.2019.00022 [arXiv:1902.06890 [hep-ph]].

[17] J. Barnard, T. Gherghetta and T. S. Ray, "UV descriptions of composite Higgs models without elementary scalars," JHEP **1402**, 002 (2014) doi:10.1007/JHEP02(2014)002 [arXiv:1311.6562 [hep-ph]].

[18] A. Hietanen, R. Lewis, C. Pica and F. Sannino, "Fundamental Composite Higgs Dynamics on the Lattice: SU(2) with Two Flavors," JHEP **1407**, 116 (2014) doi:10.1007/JHEP07(2014)116 [arXiv:1404.2794 [hep-lat]].

[19] W. Detmold, M. McCullough and A. Pochinsky, "Dark nuclei. II. Nuclear spectroscopy in two-color QCD," Phys. Rev. D **90**, no. 11, 114506 (2014) doi:10.1103/PhysRevD.90.114506 [arXiv:1406.4116 [hep-lat]].

[20] R. Arthur, V. Drach, M. Hansen, A. Hietanen, C. Pica and F. Sannino, "SU(2) gauge theory with two fundamental flavors: A minimal template for model building," Phys. Rev. D **94**, no. 9, 094507 (2016) doi:10.1103/PhysRevD.94.094507 [arXiv:1602.06559 [hep-lat]].

[21] R. Arthur, V. Drach, A. Hietanen, C. Pica and F. Sannino, "*SU*(2) Gauge Theory with Two Fundamental Flavours: Scalar and Pseudoscalar Spectrum," arXiv:1607.06654 [hep-lat].

[22] C. Pica, V. Drach, M. Hansen and F. Sannino, "Composite Higgs Dynamics on the Lattice," EPJ Web Conf. **137**, 10005 (2017) doi:10.1051/epjconf/201713710005 [arXiv:1612.09336 [hep-lat]].

[23] J. W. Lee, B. Lucini and M. Piai, "Symmetry restoration at high-temperature in two-color and two-flavor lattice gauge theories," JHEP **1704**, 036 (2017) doi:10.1007/JHEP04(2017)036 [arXiv:1701.03228 [hep-lat]].

[24] V. Drach, T. Janowski and C. Pica, "Update on SU(2) gauge theory with NF = 2 fundamental flavours," EPJ Web Conf. **175**, 08020 (2018) doi:10.1051/epjconf/201817508020 [arXiv:1710.07218 [hep-lat]].

[25] V. Drach, T. Janowski, C. Pica and S. Prelovsek, "Scattering of Goldstone Bosons and resonance production in a Composite Higgs model on the lattice," JHEP **04**, 117 (2021) doi:10.1007/JHEP04(2021)117 [arXiv:2012.09761 [hep-lat]].

[26] V. Drach, P. Fritzsch, A. Rago and F. Romero-López, "Singlet channel scattering in a Composite Higgs model on the lattice," [arXiv:2107.09974 [hep-lat]].

[27] V. Ayyar, T. DeGrand, M. Golterman, D. C. Hackett, W. I. Jay, E. T. Neil, Y. Shamir and B. Svetitsky, "Spectroscopy of SU(4) composite Higgs theory with two distinct fermion representations," Phys. Rev. D **97**, no. 7, 074505 (2018) doi:10.1103/PhysRevD.97.074505 [arXiv:1710.00806 [hep-lat]].

[28] V. Ayyar, T. Degrand, D. C. Hackett, W. I. Jay, E. T. Neil, Y. Shamir and B. Svetitsky, "Baryon spectrum of SU(4) composite Higgs theory with two distinct fermion representations," Phys. Rev. D **97**, no. 11, 114505 (2018) doi:10.1103/PhysRevD.97.114505 [arXiv:1801.05809 [hep-ph]].

[29] V. Ayyar, T. DeGrand, D. C. Hackett, W. I. Jay, E. T. Neil, Y. Shamir and B. Svetitsky, "Finite-temperature phase structure of SU(4) gauge theory with multiple fermion representations," Phys. Rev. D **97**, no. 11, 114502 (2018) doi:10.1103/PhysRevD.97.114502 [arXiv:1802.09644 [hep-lat]].

[30] V. Ayyar, T. DeGrand, D. C. Hackett, W. I. Jay, E. T. Neil, Y. Shamir and B. Svetitsky, "Partial compositeness and baryon matrix elements on the lattice," Phys. Rev. D **99**, no. 9, 094502 (2019) doi:10.1103/PhysRevD.99.094502 [arXiv:1812.02727 [hep-ph]].

[31] G. Cossu, L. Del Debbio, M. Panero and D. Preti, "Strong dynamics with matter in multiple representations: SU(4) gauge theory with fundamental and sextet fermions," Eur. Phys. J. C **79**, no. 8, 638 (2019) doi:10.1140/epjc/s10052-019-7137-1 [arXiv:1904.08885 [hep-lat]].

[32] Y. Shamir, M. Golterman, W. I. Jay, E. T. Neil and B. Svetitsky, "*S* parameter from a prototype composite-Higgs model," [arXiv:2110.05198 [hep-lat]].

[33] T. Appelquist, J. Ingoldby and M. Piai, "Nearly Conformal Composite Higgs Model," Phys. Rev. Lett. **126**, no.19, 191804 (2021) doi:10.1103/PhysRevLett.126.191804 [arXiv:2012.09698 [hep-ph]].

[34] L. Vecchi, "A dangerous irrelevant UV-completion of the composite Higgs," JHEP **02**, 094 (2017) doi:10.1007/JHEP02(2017)094 [arXiv:1506.00623 [hep-ph]].

[35] T. Ma and G. Cacciapaglia, "Fundamental Composite 2HDM: SU(N) with 4 flavours," JHEP **03**, 211 (2016) doi:10.1007/JHEP03(2016)211 [arXiv:1508.07014 [hep-ph]].

[36] D. Buarque Franzosi, G. Cacciapaglia and A. Deandrea, "Sigma-assisted low scale composite Goldstone–Higgs," Eur. Phys. J. C **80**, no.1, 28 (2020) doi:10.1140/epjc/s10052-019-7572-z [arXiv:1809.09146 [hep-ph]].

[37] Y. Aoki *et al.* [LatKMI Collaboration], "Light composite scalar in eight-flavor QCD on the lattice," Phys. Rev. D **89**, 111502 (2014) doi:10.1103/PhysRevD.89.111502 [arXiv:1403.5000 [hep-lat]].

[38] T. Appelquist *et al.*, "Strongly interacting dynamics and the search for new physics at the LHC," Phys. Rev. D **93**, no. 11, 114514 (2016) doi:10.1103/PhysRevD.93.114514 [arXiv:1601.04027 [hep-lat]].

[39] Y. Aoki *et al.* [LatKMI Collaboration], "Light flavor-singlet scalars and walking signals in N_f = 8 QCD on the lattice," Phys. Rev. D **96**, no. 1, 014508 (2017) doi:10.1103/PhysRevD.96.014508 [arXiv:1610.07011 [hep-lat]].

[40] A. D. Gasbarro and G. T. Fleming, "Examining the Low Energy Dynamics of Walking Gauge Theory," PoS LATTICE **2016**, 242 (2017) doi:10.22323/1.256.0242 [arXiv:1702.00480 [hep-lat]].

[41] T. Appelquist *et al.* [Lattice Strong Dynamics Collaboration], "Nonperturbative investigations of SU(3) gauge theory with eight dynamical flavors," Phys. Rev. D **99**, no. 1, 014509 (2019) doi:10.1103/PhysRevD.99.014509 [arXiv:1807.08411 [hep-lat]].

[42] Y. Hochberg, E. Kuflik, T. Volansky and J. G. Wacker, "Mechanism for Thermal Relic Dark Matter of Strongly Interacting Massive Particles," Phys. Rev. Lett. **113**, 171301 (2014) doi:10.1103/PhysRevLett.113.171301 [arXiv:1402.5143 [hep-ph]].

[43] Y. Hochberg, E. Kuflik, H. Murayama, T. Volansky and J. G. Wacker, "Model for Thermal Relic Dark Matter of Strongly Interacting Massive Particles," Phys. Rev. Lett. **115**, no.2, 021301 (2015) doi:10.1103/PhysRevLett.115.021301 [arXiv:1411.3727 [hep-ph]].

PoS(LATTICE2021)308

[44] Y. Hochberg, E. Kuflik and H. Murayama, "SIMP Spectroscopy," JHEP **05**, 090 (2016) doi:10.1007/JHEP05(2016)090 [arXiv:1512.07917 [hep-ph]].

[45] N. Bernal, X. Chu and J. Pradler, "Simply split strongly interacting massive particles," Phys. Rev. D **95**, no.11, 115023 (2017) doi:10.1103/PhysRevD.95.115023 [arXiv:1702.04906 [hep-ph]].

[46] A. Berlin, N. Blinov, S. Gori, P. Schuster and N. Toro, "Cosmology and Accelerator Tests of Strongly Interacting Dark Matter," Phys. Rev. D **97**, no.5, 055033 (2018) doi:10.1103/PhysRevD.97.055033 [arXiv:1801.05805 [hep-ph]].

[47] N. Bernal, X. Chu, S. Kulkarni and J. Pradler, "Self-interacting dark matter without prejudice," Phys. Rev. D **101**, no.5, 055044 (2020) doi:10.1103/PhysRevD.101.055044 [arXiv:1912.06681 [hep-ph]].

[48] Y. D. Tsai, R. McGehee and H. Murayama, "Resonant Self-Interacting Dark Matter from Dark QCD," [arXiv:2008.08608 [hep-ph]].

[49] A. Maas and F. Zierler, "Strong isospin breaking in Sp(4) gauge theory," [arXiv:2109.14377 [hep-lat]].

[50] F. Zierler and A. Maas, "*Sp*(4) SIMP Dark Matter on the Lattice," PoS **LHCP2021**, 162 (2021) doi:10.22323/1.397.0162

[51] B. Lucini and M. Teper, "SU(N) gauge theories in four-dimensions: Exploring the approach to N = infinity," JHEP **06**, 050 (2001) doi:10.1088/1126-6708/2001/06/050 [arXiv:hep-lat/0103027 [hep-lat]].

[52] B. Lucini, M. Teper and U. Wenger, "Glueballs and k-strings in SU(N) gauge theories: Calculations with improved operators," JHEP **06**, 012 (2004) doi:10.1088/1126-6708/2004/06/012 [arXiv:hep-lat/0404008 [hep-lat]].

[53] B. Lucini, A. Rago and E. Rinaldi, "Glueball masses in the large N limit," JHEP **08**, 119 (2010) doi:10.1007/JHEP08(2010)119 [arXiv:1007.3879 [hep-lat]].

[54] B. Lucini and M. Panero, "SU(N) gauge theories at large N," Phys. Rept. **526**, 93-163 (2013) doi:10.1016/j.physrep.2013.01.001 [arXiv:1210.4997 [hep-th]].

[55] A. Athenodorou, R. Lau and M. Teper, "On the weak N -dependence of SO(N) and SU(N) gauge theories in 2+1 dimensions," Phys. Lett. B **749**, 448-453 (2015) doi:10.1016/j.physletb.2015.08.023 [arXiv:1504.08126 [hep-lat]].

[56] R. Lau and M. Teper, "SO(N) gauge theories in 2 + 1 dimensions: glueball spectra and confinement," JHEP **10**, 022 (2017) doi:10.1007/JHEP10(2017)022 [arXiv:1701.06941 [hep-lat]].

[57] D. K. Hong, J. W. Lee, B. Lucini, M. Piai and D. Vadacchino, "Casimir scaling and Yang–Mills glueballs," Phys. Lett. B **775**, 89-93 (2017) doi:10.1016/j.physletb.2017.10.050 [arXiv:1705.00286 [hep-th]].

[58] N. Yamanaka, A. Nakamura and M. Wakayama, "Interglueball potential in lattice SU(N) gauge theories," [arXiv:2110.04521 [hep-lat]].

[59] A. Athenodorou and M. Teper, "SU(N) gauge theories in 3+1 dimensions: glueball spectrum, string tensions and topology," [arXiv:2106.00364 [hep-lat]].

[60] P. Hernández and F. Romero-López, "The large N_c limit of QCD on the lattice," Eur. Phys. J. A **57**, no.2, 52 (2021) doi:10.1140/epja/s10050-021-00374-2 [arXiv:2012.03331 [hep-lat]].

[61] F. Sannino, "Conformal Windows of SP(2N) and SO(N) Gauge Theories," Phys. Rev. D **79**, 096007 (2009) doi:10.1103/PhysRevD.79.096007 [arXiv:0902.3494 [hep-ph]].

[62] T. A. Ryttov and R. Shrock, "Infrared fixed point physics in SO(N_c) and Sp(N_c) gauge theories," Phys. Rev. D **96**, no.10, 105015 (2017) doi:10.1103/PhysRevD.96.105015 [arXiv:1709.05358 [hep-th]].

[63] B. S. Kim, D. K. Hong and J. W. Lee, "Into the conformal window: Multirepresentation gauge theories," Phys. Rev. D **101**, no.5, 056008 (2020) doi:10.1103/PhysRevD.101.056008 [arXiv:2001.02690 [hep-ph]].

[64] J. W. Lee, "Conformal window from conformal expansion," Phys. Rev. D **103**, no.7, 076006 (2021) doi:10.1103/PhysRevD.103.076006 [arXiv:2008.12223 [hep-ph]].

[65] T. Appelquist, P. S. Rodrigues da Silva and F. Sannino, "Enhanced global symmetries and the chiral phase transition," Phys. Rev. D **60**, 116007 (1999) doi:10.1103/PhysRevD.60.116007 [arXiv:hep-ph/9906555 [hep-ph]].

[66] E. Witten, "Current Algebra Theorems for the U(1) Goldstone Boson," Nucl. Phys. B **156**, 269-283 (1979) doi:10.1016/0550-3213(79)90031-2

[67] G. Veneziano, "U(1) Without Instantons," Nucl. Phys. B **159**, 213-224 (1979) doi:10.1016/0550-3213(79)90332-8

[68] M. Luscher, "Topology of Lattice Gauge Fields," Commun. Math. Phys. **85**, 39 (1982) doi:10.1007/BF02029132

[69] M. Campostrini, A. Di Giacomo, H. Panagopoulos and E. Vicari, "Topological Charge, Renormalization and Cooling on the Lattice," Nucl. Phys. B **329**, 683-697 (1990) doi:10.1016/0550-3213(90)90077-Q

[70] L. Del Debbio, H. Panagopoulos and E. Vicari, "theta dependence of SU(N) gauge theories," JHEP **08**, 044 (2002) doi:10.1088/1126-6708/2002/08/044 [arXiv:hep-th/0204125 [hep-th]].

[71] M. Lüscher, "Properties and uses of the Wilson flow in lattice QCD," JHEP **08**, 071 (2010) [erratum: JHEP **03**, 092 (2014)] doi:10.1007/JHEP08(2010)071 [arXiv:1006.4518 [hep-lat]].

[72] M. Lüscher, "Future applications of the Yang-Mills gradient flow in lattice QCD," PoS **LATTICE2013**, 016 (2014) doi:10.22323/1.187.0016 [arXiv:1308.5598 [hep-lat]].

[73] C. Bonanno, C. Bonati and M. D'Elia, "Large-*N* SU(*N*) Yang-Mills theories with milder topological freezing," JHEP **03**, 111 (2021) doi:10.1007/JHEP03(2021)111 [arXiv:2012.14000 [hep-lat]].

[74] S. Borsanyi and D. Sexty, "Topological susceptibility of pure gauge theory using Density of States," Phys. Lett. B **815**, 136148 (2021) doi:10.1016/j.physletb.2021.136148 [arXiv:2101.03383 [hep-lat]].

[75] G. Cossu, D. Lancastera, B. Lucini, R. Pellegrini and A. Rago, "Ergodic sampling of the topological charge using the density of states," Eur. Phys. J. C **81**, no.4, 375 (2021) doi:10.1140/epjc/s10052-021-09161-1 [arXiv:2102.03630 [hep-lat]].

[76] N. Madras and A. D. Sokal, "The Pivot algorithm: a highly efficient Monte Carlo method for selfavoiding walk," J. Statist. Phys. **50**, 109-186 (1988) doi:10.1007/BF01022990

[77] M. Cè, M. García Vera, L. Giusti and S. Schaefer, "The topological susceptibility in the large-*N* limit of SU(*N*) Yang–Mills theory," Phys. Lett. B **762**, 232-236 (2016) doi:10.1016/j.physletb.2016.09.029 [arXiv:1607.05939 [hep-lat]].

[78] M. Luscher and S. Schaefer, "Lattice QCD without topology barriers," JHEP **07**, 036 (2011) doi:10.1007/JHEP07(2011)036 [arXiv:1105.4749 [hep-lat]].

[79] L. Del Debbio, A. Patella and C. Pica, "Higher representations on the lattice: Numerical simulations. SU(2) with adjoint fermions," Phys. Rev. D **81**, 094503 (2010) doi:10.1103/PhysRevD.81.094503 [arXiv:0805.2058 [hep-lat]].

[80] G. Martinelli and Y. C. Zhang, "The Connection Between Local Operators on the Lattice and in the Continuum and Its Relation to Meson Decay Constants," Phys. Lett. B **123**, 433 (1983) doi:10.1016/0370-2693(83)90987-5

[81] G. P. Lepage and P. B. Mackenzie, "On the viability of lattice perturbation theory," Phys. Rev. D **48**, 2250-2264 (1993) doi:10.1103/PhysRevD.48.2250 [arXiv:hep-lat/9209022 [hep-lat]].

[82] B. Blossier, M. Della Morte, G. von Hippel, T. Mendes and R. Sommer, "On the generalized eigenvalue method for energies and matrix elements in lattice field theory," JHEP **04**, 094 (2009) doi:10.1088/1126-6708/2009/04/094 [arXiv:0902.1265 [hep-lat]].

[83] D. Arndt and C. J. D. Lin, "Heavy meson chiral perturbation theory in finite volume," Phys. Rev. D **70**, 014503 (2004) doi:10.1103/PhysRevD.70.014503 [arXiv:hep-lat/0403012 [hep-lat]].

[84] J. Bijnens and J. Lu, "Technicolor and other QCD-like theories at next-to-next-to-leading order," JHEP **11**, 116 (2009) doi:10.1088/1126-6708/2009/11/116 [arXiv:0910.5424 [hep-ph]].

[85] P. A. Boyle, A. Juttner, C. Kelly and R. D. Kenway, "Use of stochastic sources for the lattice determination of light quark physics," JHEP **08**, 086 (2008) doi:10.1088/1126-6708/2008/08/086 [arXiv:0804.1501 [hep-lat]].

[86] S. Gusken, "A Study of smearing techniques for hadron correlation functions," Nucl. Phys. B Proc. Suppl. **17**, 361-364 (1990) doi:10.1016/0920-5632(90)90273-W

[87] M. Albanese *et al.* [APE], "Glueball Masses and String Tension in Lattice QCD," Phys. Lett. B **192**, 163-169 (1987) doi:10.1016/0370-2693(87)91160-9

[88] P. A. Zyla *et al.* [Particle Data Group], "Review of Particle Physics," PTEP **2020**, no.8, 083C01 (2020) doi:10.1093/ptep/ptaa104

[89] G. Aarts, C. Allton, S. Hands, B. Jäger, C. Praki and J. I. Skullerud, "Nucleons and parity doubling across the deconfinement transition," Phys. Rev. D **92**, no.1, 014503 (2015) doi:10.1103/PhysRevD.92.014503 [arXiv:1502.03603 [hep-lat]].